8-2004

Design Optimization of Enriched Water Targets

Sampath Telikicherla Kandala
University of Tennessee - Knoxville

To the Graduate Council:

I am submitting herewith a thesis written by Sampath Telikicherla Kandala entitled "Design Optimization of Enriched Water Targets." I have examined the final electronic copy of this thesis for form and content and recommend that it be accepted in partial fulfillment of the requirements for the degree of Master of Science, with a major in Mechanical Engineering.

Arthur E. Ruggles, Major Professor

We have read this thesis and recommend its acceptance:

Rao V. Arimill, A. J. Baker

Accepted for the Council:
Carolyn R. Hodges

Vice Provost and Dean of the Graduate School

(Original signatures are on file with official student records.)

To the Graduate Council:

I am submitting herewith a thesis written by Sampath Telikicherla Kandala entitled "Design Optimization of Enriched Water Targets." I have examined the final electronic copy of this thesis for form and content and recommend that it be accepted in partial fulfillment of the requirements for the degree of Master of Science, with a major in Mechanical Engineering.

Dr. Arthur E. Ruggles
Major Professor

We have read this thesis

and recommend its acceptance:

Dr. Rao V. Arimill

Dr. A. J. Baker

Accepted for the council:

Anne Mayhew
Vice Chancellor and
Dean of Graduate Studies

(Original signatures are on file with official student Records)

DESIGN OPTIMIZATION OF ENRICHED WATER TARGETS

A Thesis
Presented for the
Master of Science
Degree
University of Tennessee, Knoxville

Sampath Telikicherla Kandala
August 2004

DEDICATION

I dedicate this thesis to my parents, Gopala Krishna and Mani and to my brother, Bhargav. Their constant encouragement to pursue my Masters in the USA is commendable. Without their support, this would not have been possible.

ACKNOWLEDGEMENTS

Many people have made significant and valuable contributions to this project. I thank all of them for the help they have extended. I express my utmost gratitude to my major advisor, Dr. A.E. Ruggles for accepting me to do this project. His constant support throughout this research was very encouraging. In the pursuit of my Masters degree and this project, I have learned a lot from him. The foremost thing I learned from him was the value and importance of an Engineer for a better humanity. Technical discussions with him taught me the prominence of delivering high quality results on time. Secondly, my interaction with him has helped me to hone my communication and interpersonal skills. He has motivated me to prepare this thesis and has spent several hours revising it. I am responsible for the product development starting from design concept through prototype testing which is a rare opportunity for a Masters student to get. I am thankful for it. Every stage of this project was a great challenging and an interesting learning experience. I have learned from him that all these skills coupled with diligence are necessary for an Engineer to survive in a competitive work place.

Throughout my thesis studies, I was funded by CTI Inc., Knoxville. I would like to thank Mr. Charles W. Alvord, Manager of CTI Research and Development and this project for making my Masters studies possible. I would also like to thank my thesis committee members Dr. A.J. Baker and Dr. Rao Arimilli of Mechanical, Aerospace and Biomedical Engineering Department. Their comments and suggestions are noteworthy.

Many thanks to the Head of Nuclear Engineering Department, Dr. H. L. Dodds for allowing me access to the facilities of the department. In the pursuit of my project, discussions with R. Bailey pertaining to work shop issues and with G. Graves on technical issues are very informative. Special thanks to R. Bailey and G. Graves.

Finally, I would like to thank my parents Gopala Krishna and Mani, my brother, Bhargav, and my friends, Teja, Srilalitha, Anuj, Rohan, Tina, Hari and Mohan for all their moral support and belief in me.

ABSTRACT

The purpose of this research project is to design and optimize the enriched water targets used in the cyclotron systems that are manufactured by CTI Inc. Enriched water target is the source of Fluorine 18 that is used in the Positron Emission Tomography (PET) scanners for medical imaging purposes. Oxygen 18 enriched water is the target for the 10.5 MeV protons that are produced by the cyclotron. A p-n reaction takes place when the high-energy protons interact with the Oxygen 18, creating Fluorine 18. The proton beam also deposits thermal energy in the target. As the enriched water is costly, target performance is based on the Fluorine 18 generation per gram of enriched water target. Target performance is partly determined by the heat rejection capability of the target holder. Current target designs absorb 400 Watts of power when charged with 1 cc of enriched water.

In the present research, a new design was developed with increased heat transfer capability and less inventory. The new design rejects 1000 Watts when charged with 0.7 cc of enriched water operating at 4.7 MPa (680 psia). Thermal modeling, computer simulation and experimentation supporting the design optimization are in this thesis. Future studies are also suggested. MATLAB and AutoSketch 7.0 packages are used for simulation and design rendering purposes.

TABLE OF CONTENTS

LIST OF TABLES

LIST OF FIGURES

NOMENCLATURE

A_{cd}	Surface area of the condensation dome (m^2)
A_{cond}	Heat transfer area of condensation (m^2)
A_{film}	Heat Transfer area for Condensation film (m^2)
A_{tf}	Surface area of the target front (m^2)
a_c	Cross sectional area of the fin (m^2)
b_{cd}	Base of the condensation dome, constant (m)
b_{cond}	Base of the condensation dome, varying based on vapor volume fraction (m)
b_r	Base of the ridge (m)
b_{ch}	Base of the channel (m)
g	Acceleration due to gravity (m/s^2)
h_{cond}	Condensation heat transfer coefficient ($W/(m^2\ ^oC)$)
h_f	Length of the fin (m)
h_{fg}	Latent heat of condensation of vapor (J/kg)
h_{spl}	Single-phase heat transfer coefficient ($W/(m^2\ ^oC)$)
h_{out}	Heat transfer coefficient of the process water ($W/(m^2\ ^oC)$)
k_l	Thermal conductivity of the liquid ($W/(m^oC)$)
k_s	Thermal conductivity of Silver ($W/(m\ ^oC)$)
l	Characteristic condensation length (m)

l_f	Length of the fin (m)
l_{tf}	Length of the target front (m)
P_h	Heated perimeter of cylindrical fin (m)
Pr_l	Prandtl Number of the liquid
q	Power (W)
r_{tf}	Radius of the target front (m)
sh_{cd}	Slant height of condensation dome, constant (m)
sh_{cond}	Slant height of condensation dome, varying based on vapor volume fraction (m)
t_{sat}	Saturation temperature (^oC)
t_{wall}	Wall temperature (^oC)
t_{out}	Outside process water temperature (^oC)
v_1	Volume of the target front (m^3)
v_2	Volume of forward condensation dome (m^3)
v_3	Volume of backward condensation dome (m^3)
v_4	Volume of the ridge (m^3)
v_l	Velocity of the liquid (m/s)
vh_{cd}	Vertical height of the condensation dome, constant (m)
vh_{cond}	Vertical height of the condensation dome, varying based on vapor volume fraction (m)
v_{total}	Total inventory volume (m^3)
ρ_l	Liquid density (kg/m^3)
ρ_v	Vapor density, (kg/m^3)

μ_l	Liquid viscosity (kg/(m-s))
$\propto$	Vapor volume fraction
δ	Film thickness (m)

Subscripts

c	Cross section
cd	Condensation dome
ch	Channel
cond	Condensation
f	Fin
fg	Fluid- gas mixture
film	Condensate film
h	Heated
l	Liquid
out	Outside cooling water
r	Ridge
s	Silver
sat	Saturation
spl	Single-phase liquid
t	Target
tf	Target front
v	Vapor
wall	Target wall

List of Acronyms

ANSI	American National Standards Institute
ASME	American Society of Mechanical Engineers
BL	Bypass Line
DOE	Department of Energy
EDM	Electrical Discharge Machining
FNPT	Female National Pipe Taper
MSL	Main Steam Line
NPT	National Pipe Taper
PET	Positron Emission Tomography
PWDL	Process Water Delivery Line
PWRL	Process Water Return Line
RDS	Radioisotope Delivery System
RL	Recirculation Line
SNS	Spallation Neutron Source

CHAPTER 1. INTRODUCTION

1. 1 Opportunity Description

In 2002, CTI Inc., Knoxville provided funding to the Nuclear Engineering Department to optimize the enriched water target design. Oxygen 18 enriched water is used as a target for 10.5 MeV protons to facilitate the production of Fluorine 18 used for radiopharmaceuticals injected for Positron Emission Tomography (PET) prior to scanning. These 10.5 MeV protons are produced by a cyclotron. Single clinical doses are produced to facilitate timely delivery to the patient without significant waste of product or enriched water. The target volume for production of each dose is less than 1 cc, and targets are arranged in a carousel that can position one of eight available targets in front of the proton beam.

The half-life of Fluorine 18 is 100 minutes, and the expense of enriched water encourages minimum target inventory. Optimal target performance occurs when one deposits as many protons per unit time into the target mass as possible. Current target designs rely on two-phase natural convection, requiring the water in the target to change phase to accommodate the energy deposition from the proton beam. Efficient Fluorine production requires that liquid phase enriched water remain in the path of the proton beam throughout the target exposure time. Protons of these energies are stopped in less than 2 mm in liquid water and the beam impingement area is a disk of diameter 8 mm. The ultimate heat sink for the thermal power deposited in the target is process water

circulated around the outside of the Silver target holder. The operating pressure in the current target design is maintained with Argon cover gas. Target performance is limited by the capability to reject the heat caused by the proton beam energy dissipated in the target volume. Previous target designs can reject 400 Watts from an enriched water target volume of one cubic centimeter while operating at 4.7 MPa (680 psia). Target operation pressures are limited by the strength of the proton beam access window. Current research involves water target redesign for maximum heat rejection per unit mass of enriched water in the target volume. Design optimization involves modifying the target holder geometry to enhance target material cooling while minimizing target material mass inventory.

1.2 Overview of Fluorine 18 Production

Radioisotope Delivery System (RDS) is a unit that produces radioactive Fluorine (Fluorine 18). RDS is comprised of three major components.

1) A Cyclotron: This particle accelerator produces a high-energy proton beam. The beam is accelerated into the target that is loaded with a stable chemical isotope like Oxygen 18. The proton beam from the cyclotron enters the target chamber and by means of a p-n nuclear reaction, changes the stable target material into radioactive isotope.
2) A Biosynthesizer: This component produces a variety of clinically useful radio labeled compounds. Radiopharmaceuticals produced in the cyclotron are

transferred to the biosynthesizer unit and attached to clinically useful biological markers.

3) A Computer Control Unit: This unit is used to control the cyclotron and the biosynthesizer. The desired radioisotope is selected from the menu of the computer. All other operations are carried out automatically. Once the isotope is selected, the final product is obtained without further operator intervention. This reduces personnel requirements and occupational radiation exposures. The RDS excluding the computer control unit is shown in Fig. 1.1. CTI manufactures RDS 111 and RDS Eclipse cyclotrons. These are the two cyclotron models intended for hospital and commercial use. These are capable of producing wide range of C^{11} and F^{18} based radiopharmaceuticals.

Fig. 1.1 RDS excluding computer control unit
Image source: CTI

1.3 Applications of Fluorine 18 in Medical Imaging

Fluorine 18 is used as a tracer tool for medical imaging in PET scanners. Fluorine 18 is incorporated in a sugar that is easy to metabolize. Tissue with high metabolic rate preferentially absorbs the F^{18} tagged sugar. The Fluorine 18 decays with the release of a positron. The positron then annihilates with a nearby electron to form two photons, 180^{o} apart. The photons are captured by detectors to reconstruct an image of the F^{18} distribution, which closely corresponds to metabolic rate distribution.

CLINICAL APPLICATION OF PET SCANNERS [1]

- Diagnosis and therapy management in oncology, specifically in lung, colorectal, melanoma, breast, lymphoma, head and neck cancers
- Determination of cardiac tissue viability.
- Neurological disorders particularly Alzheimer's, Parkinson's, seizures, and other dementia disorders

The PET scanner and sample scanned images are shown in Fig. 1.2.

1.4 My Contributions

My contribution to this research is optimization of the enriched water target design. Initial work involved review of prior modeling and experiments performed by Dr. Arthur E. Ruggles and Charles W. Alvord (Ruggles and Alvord, 2000). The simulation models were developed by Dr. Arthur E. Ruggles in MATHCAD and were

[1] Information from www.cti-pet.com

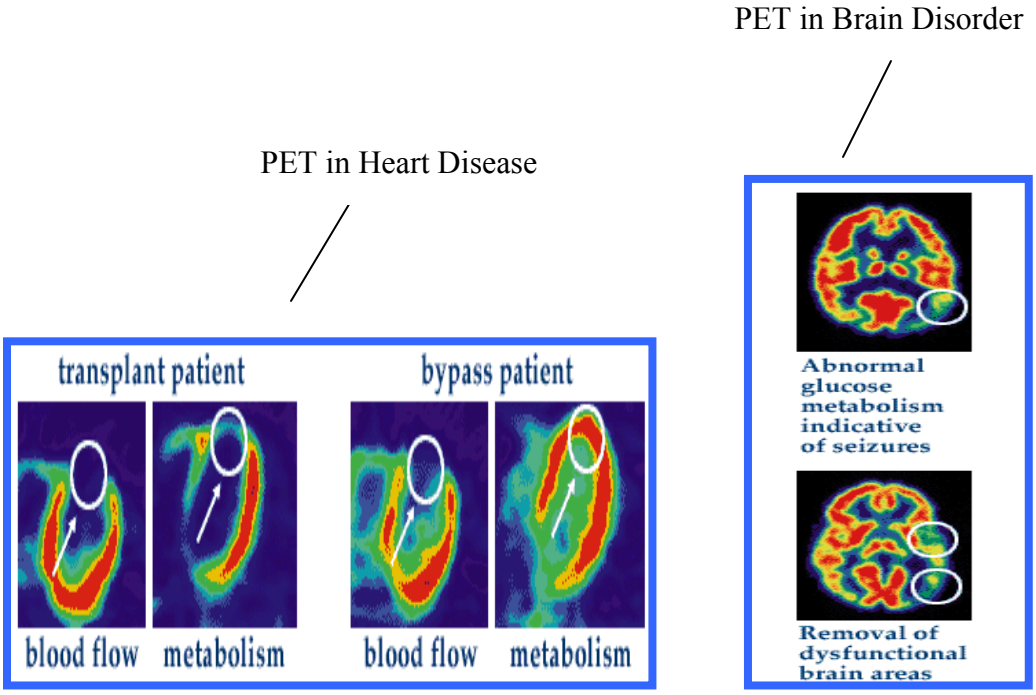

Fig. 1.2 PET scanner and the scanned images
Image Source: CTI

converted to MATLAB by J.M. Crye. This MATLAB model served as the starting point for optimization efforts in this work.

The second phase of the design involved assembling the thermal models to facilitate the optimization studies. The intended design basis for optimization is a two-phase target with a condensation dome positioned behind and slightly above the liquid region where the beam impingement occurs. This type of target is referred to as a reflux target by those in the industry. The models were assembled in software that allows the evaluation of the thermal performance of a target as a function of the target volume. Models were included that predict the fluid film thickness and volume fraction associated with condensation. The software allows one to specify, by function or tabulation, the relationship between the vapor volume fraction and the heat transfer area available for condensation. The relationship between target power and vapor volume fraction is part of the program output, along with evaluations of the liquid and vapor mass inventory.

The third phase of the design focuses on a baseline mass inventory of one gram of enriched water. Geometries were chosen and the relationship between the vapor volume fraction and the area for condensation was formulated. The relationship between the characteristic length of the draining film and the vapor volume fraction is also derived for the new geometry. These models combine to allow simulation of the target performance. Software developed in phase 2 has been exercised and refined to provide optimized target geometry from the baseline. The power attributable to the new geometry using the baseline inventory can then be established. Geometric perturbations were conducted until a near optimum design was achieved. The new reflux target design absorbs 1,000 Watts of beam power when charged with 0.7 cc of enriched water and

operating at 4.7 MPa (680 psia). The extension of the target power to higher values will make the performance of the target holder heat sink more important.

The fourth phase of the effort involves experimentation to test the thermal performance of the reflux target holder heat sink. This experiment evaluates the target performance for a range of operating pressures and process water flow rates. The experiment was designed and built in the Nuclear Engineering Department of The University of Tennessee, Knoxville. Each design phase is discussed in detail in the following chapters.

CHAPTER 2. REVIEW OF PRIOR WORK

The following sections describe the basic thermal performance attributes of the CTI Oxygen 18 enriched water target that were simulated using integral control volume methods (Ruggles and Alvord, 2000). These models are in agreement with data taken from a target subjected to a range of beam powers. The target simulation integrates heat transfer models for condensation and two-phase natural convection.

2.1 The Target Volume Thermal Model

Figure 2.1 shows the target holder and the target volume. The target volume is modeled as a circular cylinder of radius 0.0059 m and 0.008 m in length. The forward face of the cylinder faces the beam and is defined by a beam window. The beam window is cooled by Helium external to the target volume and this face is taken to be adiabatic in this simulation. The remaining surfaces of the target volume are adjacent to the silver target holder. The dimensions for the current target are given in table 2.1. The target average volumetric heating was evaluated by dividing the beam power by the total target volume. The target average volumetric heating is 460 MW/m^3, which is just over half of the peak volumetric heating of 800 MW/m^3 expected in the Spallation Neuton Source (SNS) currently being developed by the U. S. Department of Energy (DOE).

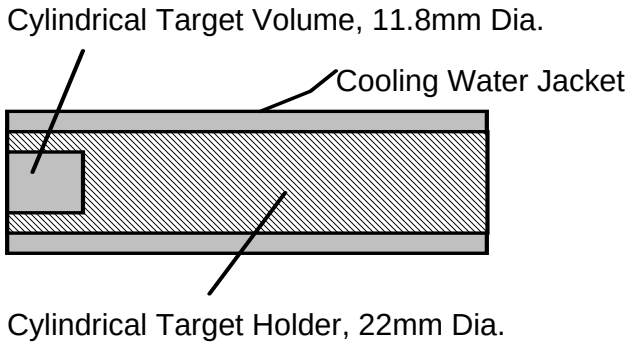

Fig. 2.1 Schematic of water target volume in Silver target holder

Table 2.1 Current target geometry dimensions

Diameter of the target holder	0.022 m
Length of the target holder	0.076 m
Diameter of the target	0.012 m
Length of the target	0.008 m
Heat transfer area to the Silver target	3.7492×10^{-4} m^2
Silver target volume	8.7443×10^{-7} m^3

The 10.5 MeV protons deposit their energy within the first 1.5 mm of travel in liquid water, so the peak volumetric heating in the CTI target exceeds that in the SNS. The average surface heat flux is evaluated by dividing the beam power by the heat transfer area, where the heat transfer area is the area of the cylinder including just one end. The average surface flux at the interface between the target and the target holder is 1.0 MW/m^2. As a reference, the heat flux that causes a transition from nucleate boiling to film boiling (so-called critical heat flux) in water at one atmosphere is roughly 1.0 W/m^2.

2.1.1 Maximum Single-Phase Power

It is also useful to estimate the maximum power the target can absorb without creating vapor. A representative heat transfer coefficient for single-phase natural convection to water in an enclosed volume similar to the target volume is 400 $W/(m^{2o}C)$. The saturation temperature for the target water is 260^oC, and the minimum temperature in the system is the heat sink process water, which is taken as 40^oC in this simulation. These assumptions allow for an estimation of the maximum power the target volume can reject without creating vapor as 33 Watts. Note that vapor production is expected at lower power due to the peaking of the beam energy deposition in the forward center of the target volume. The peak volumetric energy deposition causes rapid volumetric heating which would likely lead to vapor production prior to the power level predicted above.

2.1.2 Condensation Heat Transfer Coefficient and Condensation Power

The target is assumed to be horizontally mounted with the top volume of the target filled with vapor and the bottom filled with liquid. The vapor phase and the liquid phase are assumed to be at saturation. The heat transfer between the portion of the target volume filled with vapor and the target holder is evaluated using models for laminar falling film condensation. A model for the laminar falling film condensation heat transfer coefficient, h_{cond}, developed by Nusselt (Nusselt, 1916) was taken.

$$h_{cond} = 1.13 \frac{\left[\rho_l (\rho_l - \rho_v) g \cdot h_{fg} \cdot k_l^3\right]^{1/4}}{\left[l \cdot \mu_l \cdot (t_{sat} - t_{wall})\right]^{1/4}} \tag{2.1}$$

where, ρ is density, g is gravitational acceleration, h_{fg} is the latent heat of evaporation, k_l is the liquid conductivity, l is a characteristic length, μ_l is the liquid viscosity, t_{sat} is the saturation temperature, and t_{wall} is the wall temperature. All units are SI and properties are taken for standard (i.e., not enriched) water saturated at 260^{o}C. The characteristic length for the condensate film is taken as 0.005 m, roughly the target radius, and the behavior of the condensation heat transfer coefficient is given in Fig. 2.2. The power attributable to condensation heat transfer is given in Fig. 2.3 as a function of wall temperature for the case where half of the target volume is occupied by vapor.

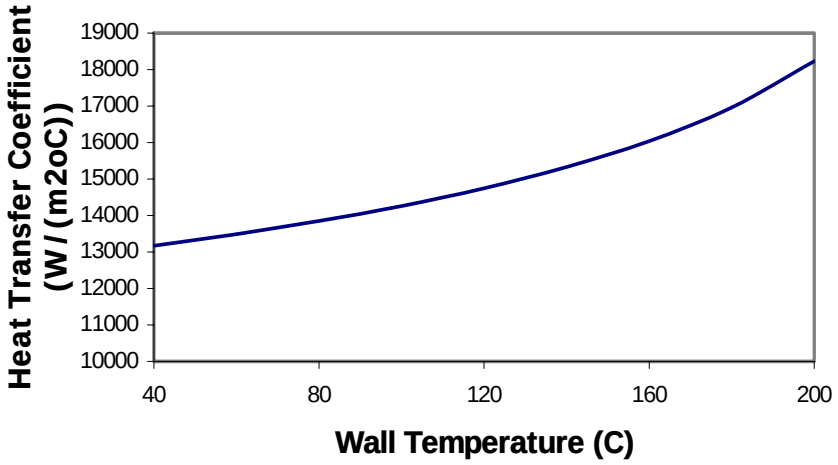

Fig. 2.2 Condensation heat transfer coefficient as a function of target wall temperature

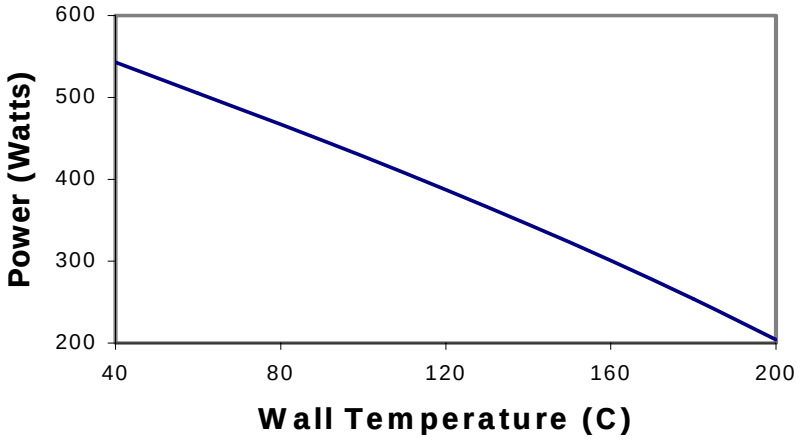

Fig. 2.3 Power attributable to condensation heat transfer at 50% vapor volume

2.1.3 Single Phase Heat Transfer Coefficient and Single Phase Power

The single-phase heat transfer coefficient was estimated by starting with the calculation of liquid velocity. The vapor volume production rate was used to estimate the average liquid velocity in the target. It was assumed that the vapor flows in the forward region of the target and occupies half of the target volume. If all the beam power is used to generate vapor, then the vapor mass generation rate is given by the beam power divided by the latent heat of evaporation. The vapor volume generation rate is evaluated as the mass generation rate divided by the vapor density as 2.4×10^{-4} m^3/s. This indicates that vapor volume equal to just over eleven times the total target volume is produced each second if single-phase heat transfer to the target holder is ignored. This produces a liquid velocity of 0.215 m/s and facilitates approximation of the heat transfer coefficient between the liquid portion of the target and the target holder. An alternate approach for finding the liquid velocity is to use the basic displacement and velocity equations. The displacement for this calculation will be the characteristic length, 0.005 m. From s= v t & v = at, the displacement over a certain time period is given as,

$$s = \int_0^t \frac{ds}{dt} dt = \int_0^t v\, dt = \int_0^t a\, t\, dt = a\frac{t^2}{2} \tag{2.2}$$

Performing algebra and substituting s = 0.005 m and g = 9.81 m/ s^2, eq 2.2 gives t=0.03 s. Substituting time and displacement gives the liquid velocity as 0.2 m/sec. Dittus and Boelter equation (Dittus, F. W., and L. M. K. Boelter, 1930) equation was employed for the single phase forced convection heat transfer coefficient, h_{spl}.

$$h_{sgl} = \frac{k_l}{l} 0.023 \left(\frac{\rho_l \cdot v \cdot l}{\mu_l} \right)^{0.8} (\mathrm{Pr}_l)^4 . \tag{2.3}$$

The power attributable to heat transfer between the liquid and the target holder when the liquid occupies half of the target volume is given in Fig. 2.4.

2.1.4 Total Target Power and Power Ratio for Different Vapor Volume Fractions

The inner wall temperature of the target holder, T_{wall}, is taken as uniform. This is due to the silver conductivity of 400 W/(m^{o}C), which makes the target holder quite effective in conducting thermal power.

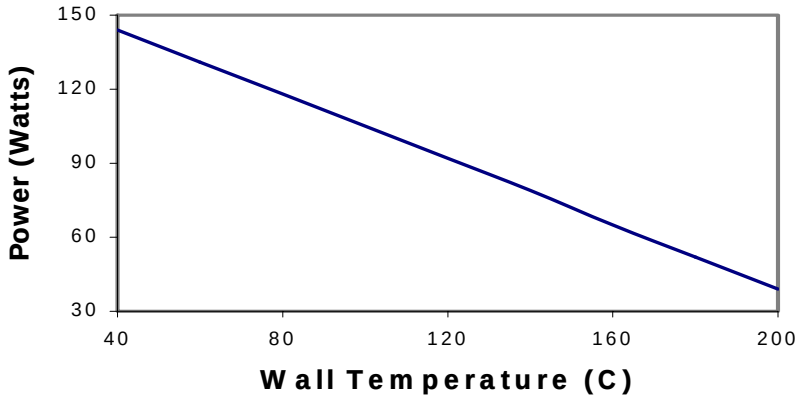

Fig. 2.4 Power attributable to single-phase heat transfer at 50% vapor volume

The one-dimensional temperature gradient in the silver target holder due to an applied flux of 1.0 MW/m^2 is 25^{o}C/cm. This indicates the target inner wall temperature is not likely to vary by more than 25^{o}C for the nominal operating condition where such flux is average. The target performance was studied with vapor occupying 20 %, 50 % and 70 % of the target volume in the previous modeling effort by Ruggles and Alvord, 2000.

2.2. Target Holder Thermal Model

The silver target holder is modeled as a single cylindrical fin with a base temperature equal to the inner wall temperature of the target. The outer circumference of the target holder is cooled with process water of temperature 40^{o}C. The power transferred from the fin, q_f, is given as,

$$q_f = m_a (t_{wall} - t_{out}) \tanh\left(m_f l_f\right) \tag{2.4}$$

where,

$$m_a = \left(h_{out} P_h k_s a_c\right)^{1/2} \tag{2.5}$$

and,

$$m_f = \left[\frac{h_{out} P_h}{k_s a_c}\right]^{1/2} \tag{2.6}$$

where, parameter P_h is the perimeter of the target holder, a_c is the cross-sectional area of the target holder, h_{out} is the external heat transfer coefficient and k_s is the conductivity of silver.

2.2.1 Target Holder External Heat Transfer Coefficient

The heat transfer coefficient between the process water and the outer surface of the target holder, h_{out}, is difficult to evaluate. The outer circumference of the target holder is threaded with eight threads per inch. The threads are nominally 2.1 mm deep and form the flow channel for the process water. The outer diameter of the target holder is 25.2 mm and slips into a smooth bore in the target holder carousel with clearance of around 0.25 mm. Significant flow will leak through the clearance between the outer diameter of the target and the inner diameter of the target carousel bore. Secondary flows are to be expected in the process water flow inside the spiral threads. All these complications motivated a bounding calculation, with the minimum external heat transfer coefficient, h_{out}, taken as 5,000 W/(m^{2o}C) and the maximum value taken at 10,000 W/(m^{2o}C). This takes into consideration of uniform external heat transfer coefficient value. The target holder outer diameter is taken at 22 mm. The length of the target holder as a fin, l_f, is taken as 76 mm. Figure 2.5 shows the target holder power as a function of target volume inner wall temperature for the two bounding external heat transfer coefficient values. As shown from Fig. 2.5, the power rejected by the target holder to the process water is higher for greater heat transfer coefficient which indicates the prominence of greater heat transfer coefficients. Target holder external heat transfer coefficient model has to be modified if the external geometry is modified. Also, the heat transfer coefficient changes dramatically if the pressure drop of the process water flow varies across the length of the target holder external surface.

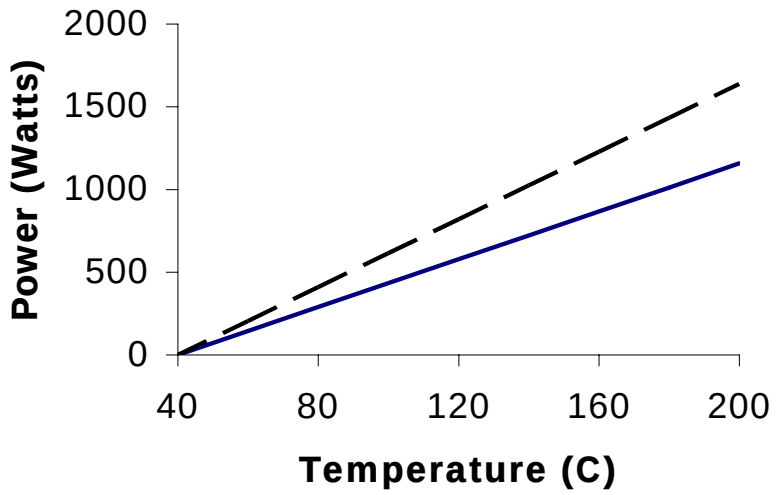

Fig. 2.5 Target holder power rejected to process water as a function of target volume inner wall temperature. Dashed line for 10,000 W/(m^{2o}C), solid for 5,000 W/(m^{2o}C).

2.3 Target Thermal Model Integration and Comparison with Data

The target holder thermal model and the target volume thermal model have the target volume inner wall temperature as a common parameter. These models are solved simultaneously for the power value that matches the target volume inner wall temperature. The target power is given as a function of the target vapor volume fraction in percent in Fig. 2.6 for the two bounding values of target holder external heat transfer coefficient. Data taken from a target subjected to a range of beam power values with provision for measurement of the displaced liquid volume are also presented on Fig. 2.6.

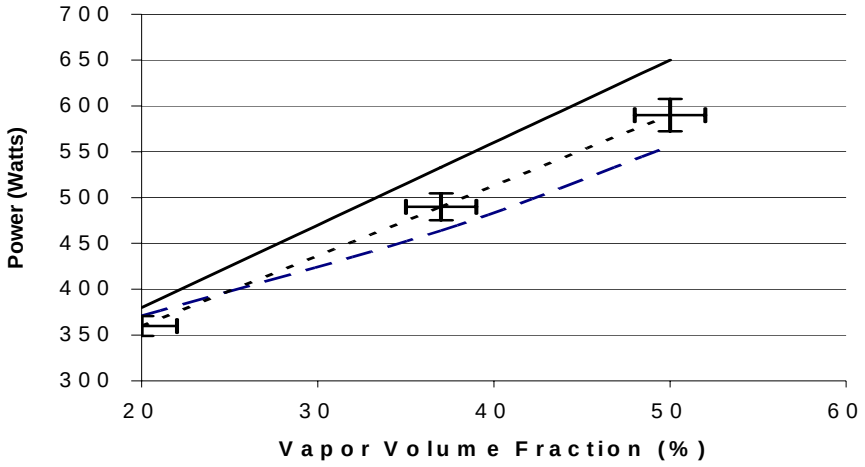

Fig. 2.6 Target power versus vapor volume fraction in percent. Solid line is model with external heat transfer coefficient equal 10,000 W/(m^{2o}C), dashed line is model with external heat transfer coefficient equal 5,000 W/(m^{2o}C), data line presented with error bars

CHAPTER 3. HIGH PERFORMANCE ENRICHED WATER TARGETS

Target and target holder thermal models developed in chapter 2 were assembled in a manner so that the user can control the target thermal performance by altering the operating conditions and the geometric dimensions. The program with those models is given in Appendix A. Models used in this program are for a cylindrical target and the dimensions used are of the RDS-111 target. Inventory management studies were performed to aid the new design by including models for condensate film thickness and condensate film area. Models were also developed to allow evaluation of vapor mass since a major portion of the target volume in the optimized design is attributed to vapor.

3.1 Inventory Based Optimization Program

The MATLAB software developed by J.M. Crye was modified and the models were assembled into a format that facilitates design optimization studies. The new software allows the evaluation of the thermal performance of a target as a function of the target volume. The three principal components of the liquid inventory include the portion absorbing beam energy, the portion in the draining condensate film, and the condensate in transit between the draining film and the beam impingement volume. The mass of the vapor constitutes the remaining portion of the target mass inventory. The algorithms followed by J.M.Crye program and the inventory based optimization program is given in

Appendix A. Models are included that predict the fluid film thickness and volume fraction associated with condensation. Target mass inventory models were added. These models are discussed in the following section.

3.2 Condensate Film: Thermal Modeling and Liquid Volume

Models to predict condensate film thickness, film area and film volume are incorporated in the program. The three heat transfer models used to study the condensate film inventory are given below.

For credible flux, and these film lengths, the Re_{film} is very much laminar. The condensate film thickness for a laminar falling film as given by Nusselt and taken from (Holman, 1997) is,

$$\delta_{film} = \left[\frac{4 \cdot \mu_l \cdot l \cdot k_l \cdot (t_{sat} - t_{wall})}{h_{fg} \cdot g \cdot \rho_l \cdot (\rho_l - \rho_v)} \right]^{1/4} \tag{3.1}$$

Figure 3.1 shows the required film thickness to get the desired target power. The film thickness at 700 Watts is 6.65 x 10^{-5} m. From eq. 3.1, for a given target power, the film thickness increases as the characteristic length increases. Since the conductivity of the liquid is of the order 0.6 W/(m^{o}C), the heat transfer coefficient goes down as δ_{film} increases. The characteristic length associated with the draining must be short to promote high heat transfer coefficients. This is an important observation for the design.

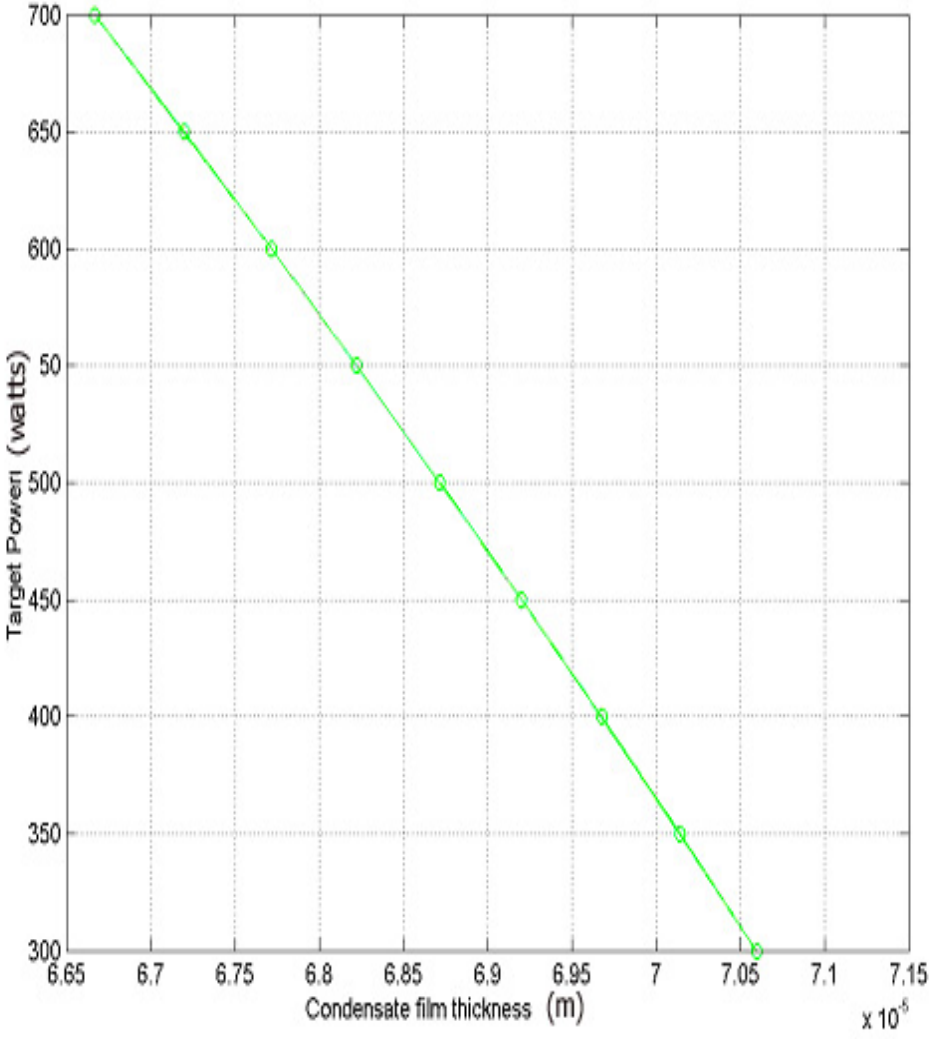

Fig. 3.1 Variation of condensate film thickness with target power

The condensate film area is modeled as the area available for condensation and is given as

$$A_{film} = A_{silver} * \alpha \tag{3.2}$$

MATLAB results are given in Fig. 3.2. Condensate film area increased from 0.5 x 10^{-4} m^2 to 2.85 x 10^{-4} m^2 as the power increased from 300 Watts to 700 Watts.

The condensate film volume is the product of condensate film thickness and condensate film area. Results from MATLAB show that at 700 WATTS, the vapor volume fraction is just 2 % of the total target volume, but it contributes more than 70 % of the local heat transfer.

3.3 Summary of Simulation Behavior

The liquid inventory in the condensate film grows as the length of the target is extended. The inventory associated with transporting condensate back to the beam impingement volume also grows with increasing target length. From these evaluations, it can be concluded that the surface area of the condensation dome should be increased to increase target power. The drain length for the film should be minimized. Length along the beam axis should not be so long that the velocity of the vapor entering the dome impedes the return of liquid to the beam strike.

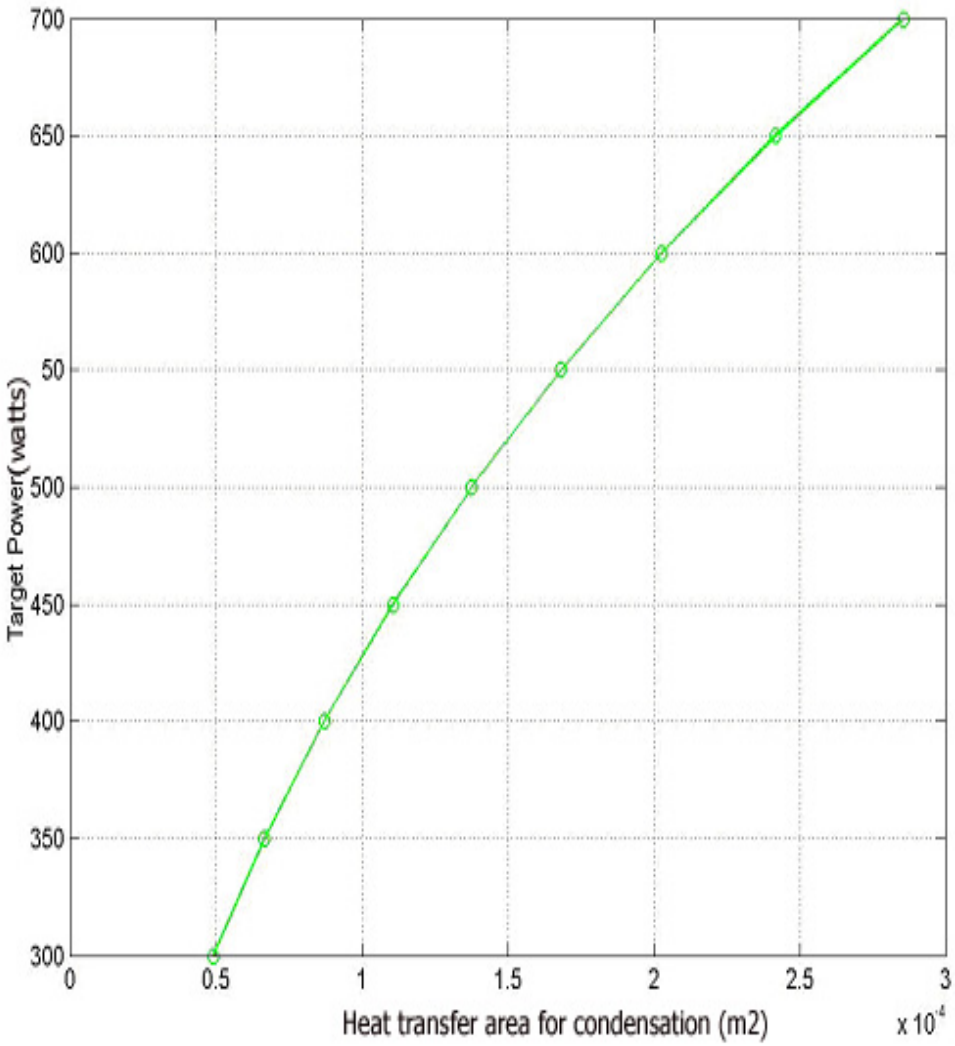

Fig. 3.2 Variation of condensate film area with target power

3.4 Design of Reflux Target

The intended design basis for optimization is a reflux target with the condensation dome positioned behind and slightly above the region of beam impingement, as shown in Fig. 3.3. This design avoids having the vapor flow opposite to the draining film of condensate, which thickens the liquid film and inhibits heat transfer to the target holder. The liquid inventory in the condensate film grows as the length, L_c, of the condensation dome is extended. The inventory associated with transporting condensate back to the beam impingement volume also grows with increasing L_c.

3.5 Selection of Target Geometry

Certain design constraints guide the derivation of target geometry. Target volume and target load mass are not directly connected. A liquid disc of 2 mm thickness and 10 mm diameter must be available in the target front to stop the beam. This protects

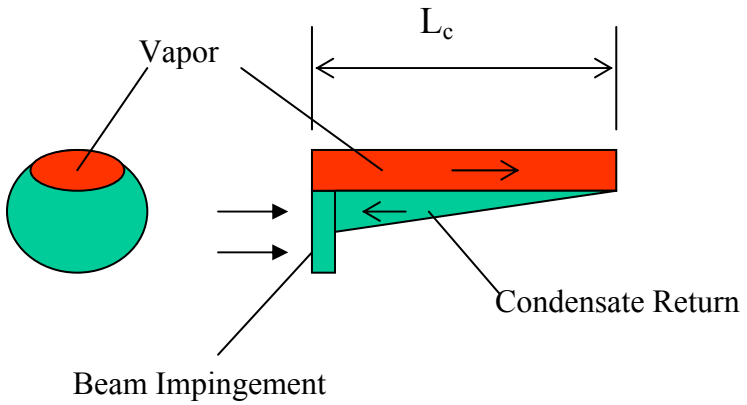

Fig. 3.3 Baseline target volume for optimization

the target holder from activation by the high-energy photon beam. Long vertical dimensions in the condensation regions are avoided as they contribute to film thickening that decreases the condensation heat transfer coefficient. The velocity of vapor in the front of the target condensation region must be limited to allow liquid return flow. Utilization of a conventional production target holder and carousel system with fixed outer dimensions is economically advantageous. Only inner dimensions of the target holder are modified in the new design.

In order to satisfy the design constraints, the target geometry should have a beam stop region and a condensation dome. The beam stop region is filled with single-phase liquid whereas the condensation dome contains the condensate liquid film, water vapor, and water in transit from the condensate film to the region of the beam energy dissipation. The reflux target geometry chosen for heat transfer models derivation and MATLAB simulation is presented in Fig. 3.4. This reflux target geometry has a semicircular beam stop region with a ridge running parallel to the beam axis. The importance of ridge is described in chapter 4. The triangular regions in the condensation dome are taken as equilateral for easy modeling and manufacturing. Heat transfer models are updated for the reflux geometry using the geometric relations given in Fig. 3.4. Target front is the beam stop region and the front region of the condensation dome excluding the ridge. The remaining portion of the target volume constitutes the volume of the condensation dome.

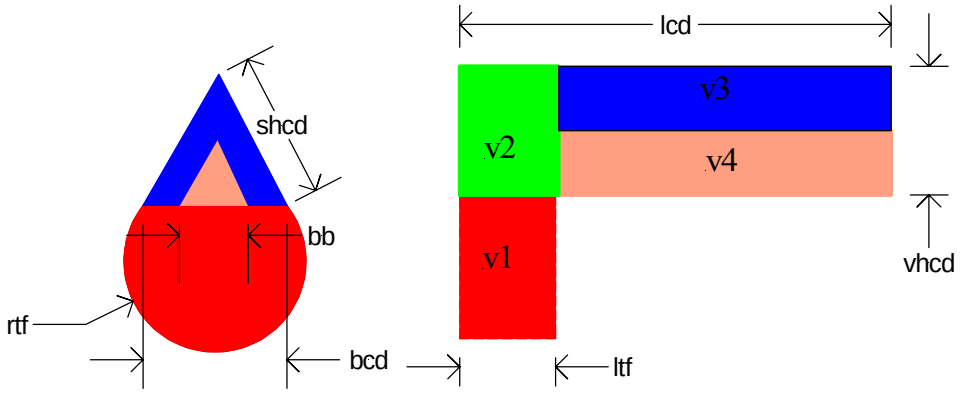

Fig. 3.4 Target geometry showing different volumes

* The two triangles bounding the condensation dome are equilateral such that $b_{cd}=sh_{cd}$, $vh_{cd}=0.866b_{cd}=0.866sh_{cd}$, $bcond=sh_{cond}$, $vh_{cond}=0.866\ b_{cond}=0.866\ sh_{cond}$. These relations simplify the algebra in calculating the heat transfer areas. Volumes in figure are defined as v_1: volume of the target front; v_2: volume of forward condensation dome; v_3: volume of backward condensation dome; v_4: volume of ridge; $v_2 + v_3 - v_4$: volume of the condensation dome

3.6 Thermal Model Development

Heat transfer area models for the new geometry are derived using the energy balance equations. Energy transport models between the target and target holder were balanced with models for the energy transfer between the target holder and the cooling water to give target inner wall temperatures. The power the target transfers to the target holder is divided into that attributable to single-phase convection and film-wise condensation. The vapor volume is evaluated by relating the required heat transfer area for condensation to the associated vapor volume using geometric relationships. The maximum power is dissipated for a given geometry when the condensation dome is completely filled with vapor while maintaining the minimum liquid for beam stop.

3.6.1 Target Wall Temperature Model

The Energy transfer between the target and target holder must balance the energy transfer between the target holder and process water. This balance was used to solve for the inner wall temperature of the target holder. The fin models are similar to those used in section 2.2.

3.6.2 Vapor Volume Fraction Model

Calculation of vapor volume fraction involves equating the beam power to the total power transfer due to single-phase convection and condensation heat transfer. The condensate film is laminar and heat transfer between the single-phase liquid and the target inner wall is by forced convection. The general formulae for single-phase and

condensation heat transfer coefficients from chapter 2 are applicable for the new reflux target, except for the heat transfer areas. Fig. 3.4 shows the division of volumes and the corresponding surface areas for heat transfer of the new reflux target. It is considered that the surface area of target front, A_{tf}, corresponding to the beam stop volume, v_1, always contributes to single-phase power from target to the target holder. The total surface area of the condensation dome, A_{cd}, corresponds to volumes v_2, v_3 and v_4 as shown in Fig. 3.4. Condensation heat transfer area, A_{cond}, is the portion of the condensation dome area available to condensation, which depends on the vapor volume occupying the condensation dome. The contribution of the condensation dome to the single-phase heat transfer area is given by $A_{cd} - A_{cond}$. Therefore, the effective single-phase heat transfer area is $A_{tf} + A_{cd} - A_{cond}$. For maximum power, vapor occupies the entire condensation dome and the effective single-phase heat transfer area is A_{tf}. By adding condensation and single-phase powers and substituting the corresponding heat transfer areas, the target power, q_t, is given as,

$$q_{spl} = h_{spl} \cdot (A_{tf} + A_{cd} - A_{cond}) \cdot (t_{sat} - t_{wall}) \tag{3.3}$$

$$q_{cond} = h_{cond} \cdot A_{cond} \cdot (t_{sat} - t_{wall}) \tag{3.4}$$

$$q_t = q_{spl} + q_{cond} \tag{3.5}$$

All the terms in the eq. 3.3 and eq. 3.4 are known except for the condensation heat transfer area, A_{cond}. Condensation heat transfer area, A_{cond}, varies with the vapor volume fraction, α. For lower beam powers, the vapor occupies the regions above the ridge whereas for higher beam powers vapor occupies the regions below the ridge. Models for heat transfer area and vapor volume as a function of beam power are necessary to evaluate target performance during start-up and shutdown transients. Calculating condensation heat transfer area, A_{cond}, in terms of vapor volume fraction, α, and substituting in eq. 3.5 produces vapor volume fraction, α, for that particular beam power.

Lower Beam Power Model

This evaluation was done for vapor occupying the regions just above the ridge as shown in Fig. 3.5. Fig. 3.5 shows the maximum vapor occupied in this region. The volume occupied by the vapor is given as,

$$v_{total} = \alpha . 0.5 . b_{cond} . h_{cond} . l_f \tag{3.6}$$

Simplifying the above equation for base, b_{cond}, and using the data from Fig. 3.4 gives,

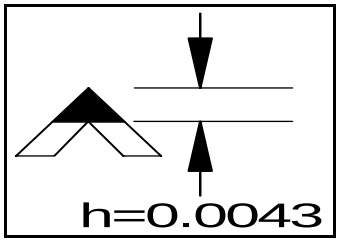

Fig. 3.5 Vapor occupying the regions above the ridge

$$b_{cond} = \left[\frac{2.\alpha.v_{total}}{0.866.l_f} \right]^{1/2} \tag{3.7}$$

Since the surface area available for condensation is the 2 slant edges of the condensation dome, l_f, the available surface area for condensation, A_{cond}, is given as,

$$A_{cond} = (2 . sh_{cond}) . l_f = 2 . b_{cond} . lf \tag{3.8}$$

Substituting eq. 3.7 in eq. 3.8 and equating the result to eq. 3.5 gives,

$$\alpha = \frac{0.866 . l_f}{2 . v_{total}} \left\{ \frac{q_t - \left[h_{spl} \left(t_{sat} - t_{wall} \right) \left(A_{tf} + A_{cd} \right) \right]}{2 . l_f . \left(h_{cond} - h_{spl} \right) \left(t_{sat} - t_{wall} \right)} \right\}^2 \tag{3.9}$$

The above formula gives the vapor volume fraction,α, for lower powers.

Higher Beam power Model

This evaluation considers the vapor occupying the regions below the ridge for higher beam powers. Figure 3.6 below shows the vapor volumes that extend below the ridge. The ridge complicates the geometrical constrains in the model derivation but the approach for the vapor volume fraction evaluation remains the same. From Fig 3.4, the affect of the ridge on the relationship between vapor volume and target dimensions is given as,

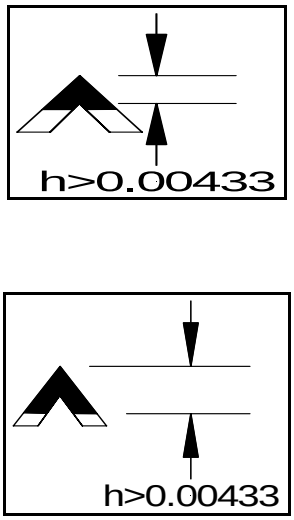

Fig. 3.6 Vapor occupying the regions below the ridge

$$\alpha.v_{total} = [(0.5 b_{cond} . 0.866 b_{cond} . (l_f - l_{tf})) + (0.5 b_{cond} . 0.866 b_{cond} . l_{tf}) - (0.5 b_r . 0.866 b_r (l_f - l_{tf})] \quad (3.10)$$

Solving for b_{cond}, gives,

$$b_{cond} = \left[\frac{\alpha . v_{total}}{0.433 . (l_f - l_{tf}) + (0.433 . lt_f) - 0.10825 (l_f - l_{tf})} \right]^{1/2} \quad (3.11)$$

The surface area available for condensation also changes and is given as,

$$A_{cond} = (2 . sh_{cond} . l_{tf} + 2 . sh_{cond} + 2. b_{ch} + 2. b_r) . (l_f - l_{tf}) \quad (3.12)$$

Substituting eq. 3.11 in eq. 3.12 and using data from Fig 3.4. leads to,

$$A_{cond} = \left(0.006 + 4l_{f} + 4l_{tf}\right)\left[\frac{\alpha \,.\, v_{total}}{0.32475\, l_{f} + 0.10825\, l_{tf}}\right]^{1/2} \tag{3.13}$$

Equating eq. 3.13 to eq. 3.5 and solving for $\propto$ gives,

$$\alpha = a\ b \tag{3.14}$$

where,

$$a = \left\{\frac{\left[q_{t} - \left(h_{spl}\left\{t_{sat} - t_{wall}\right\}\left\{A_{tf} + A_{cd}\right\}\right)\right]}{\left(h_{cond} - h_{spl}\right)\left(t_{sat} - t_{wall}\right)\left(0.006 + 4\,l_{f} - 4\,l_{tf}\right)}\right\}^{2}$$

$$b = \left(\frac{0.32475\, l_{f} + 0.10825\, l_{tf}}{v_{total}}\right)$$

The above formulae will give the vapor volume fractions for higher powers.

3.6.3 Condensate Film Area Model

The vapor after condensing flows down the walls of the dome and reaches the return channels. The vapor volume fractions calculated above are used for the calculation

of film area. Condensation heat transfer area, A_{cond}, is same as the condensate film area, A_{film}.

Film Area for Low Vapor Volume Fraction

After evaluating the vapor volume fraction, substituting eq. 3.7 in eq. 3.8 gives,

$$A_{film} = 2 l_f \cdot \left[\frac{\alpha \cdot v_{total}}{0.866 l_f} \right]^{1/2} \tag{3.17}$$

Film Area for High Vapor VolumeFfractions

Similarly using the data in Fig 3.4. and substituting eq. 3.11 in eq. 3.12 gives,

$$A_{film} = (4 l_f - 2 l_{tf}). \left[\frac{\alpha \cdot v_{total}}{1.56 l_f} \right]^{1/2} \tag{3.18}$$

3.6.4 Condensate Film Thickness Model

For laminar falling film condensation, the condensate film thickness, δ, used in section 3.2 was used. The film thickness, δ, is taken times the film area, A_{film}, to evaluate the liquid inventory associated with the condensate films.

3.6.5 Return Volume Model

The condensate flows down the walls of the condensation dome and forward through the return channels to the beam stop region. The volume of liquid in the return channels is given as the total inventory volume, v_{total}, less beam stop volume, vapor

volume and the condensate film volume. The next chapter describes the performance and specifications of the optimized target design. Software attached in Appendix B on these new models. Design iterations are performed by varying the target dimensions and the final optimized target design is presented in next chapter.

CHAPTER 4. OPTIMIZED ENRICHED WATER TARGETS

4.1 Design of the Target Geometry

Software described in chapter 3 has been exercised and refined to provide optimized target geometry from the baseline. An auto sketch rendering of the optimized design is given in Fig. 4.1. This section describes the design constraints and the target geometry description. Dimensions of the optimized target are given in table 4.1

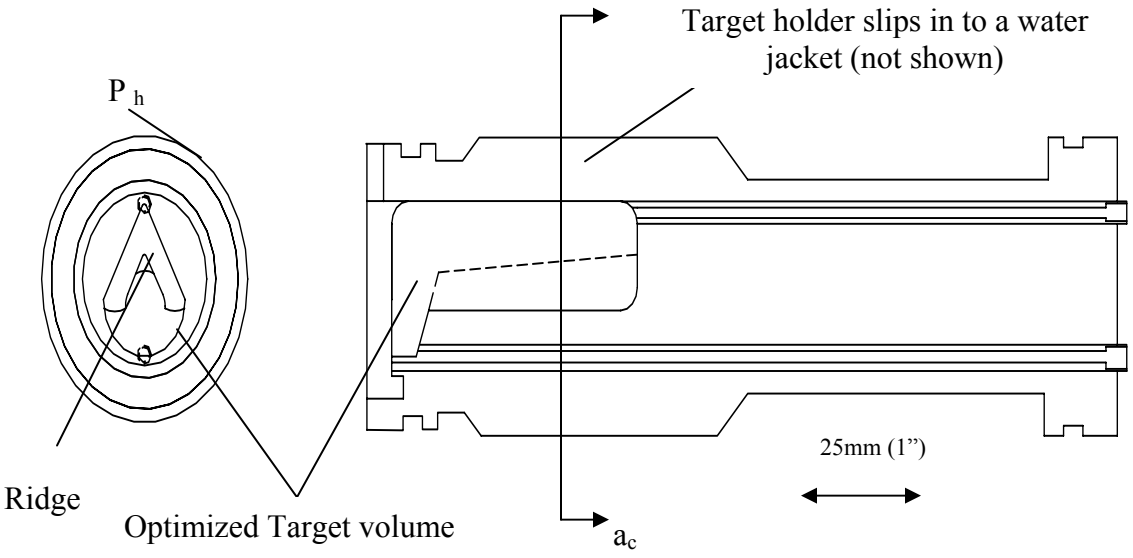

Fig. 4.1 Optimized target volume, based on RDS 111 target holder

Table 4.1 Optimized target geometry dimensions

Dimension	Value
Radius of the beam stop region	0.0075 m
Length of the beam stop region	0.0045 m
Length of the Target front	0.0015 m
Slant height of the condensation dome	0.0405 m
Length of the condensation dome	0.0405 m
Height of the condensation dome	0.0129 m
Base of the condensation dome	0.0150m
Length of the ridge	0.0405 m
Slant height of the ridge	0.0075 m
Height of the ridge	0.0060 m
Base of the ridge	0.0075 m
Target geometry volume	1.6800 cc
Total heat transfer area	0.002475 m^2
Beam stop volume	0.2400 cc
Vapor volume	1.1760 cc
Condensate volume	0.0018 cc
Return Volume	0.2622 cc

4.2 Thermal Performance of the Optimized Target

The liquid volume required to absorb the beam is taken to be that of a disk of diameter 10 mm and thickness 2 mm, giving a total volume of 0.16 cc. The remainder of the target inventory is available for heat transfer to the target holder. The optimized design will absorb 1,000 Watts of beam power when charged with 0.7 cc of enriched water and operating at 4.7 MPa (680 psia). The method of target charging and the method for target pressure control (e.g., argon cover-gas volume) will need to be modified to attain these operating conditions. The target will have a vapor volume fraction of roughly 80% ± 5% during full power operation due to the large volume and area dedicated to condensation.

The condensation volume now includes a ridge running parallel to the target holder major axis on the lower surface. This ridge uses liquid surface tension and gravity to perform as a heat transfer surface. This approach has been explored to enhance commercial condenser performance (Van Carey, 1992). Surface tension pulls the liquid away from the top of the ridge, denoted by number one in Fig. 4.2, due to the curvature of the interface. Alternately, surface tension encourages the liquid to pool at the bottom of the troughs formed to the left and right of the ridge, denoted by number two in Fig. 4.2, which serve as the condensate return channels. The center ridge significantly enhances the area available for vapor condensation per unit target vapor volume. The characteristic length of the cross-section of the condensation region in this design is roughly 4 mm, increasing the importance of surface tension on the fluid behavior and vapor orientation.

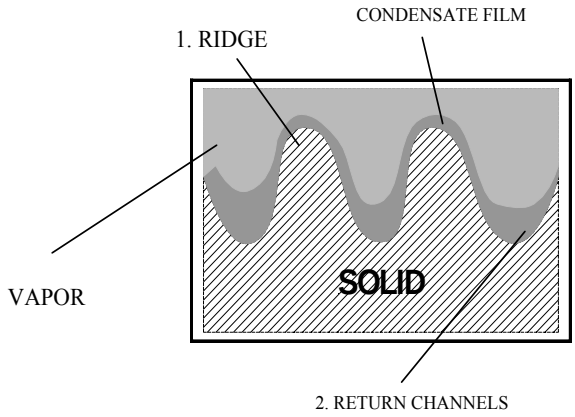

Fig. 4.2 Operation of the condenser fin on the bottom of the condensation volume

The current design for the condensation region shares attributes with the so-called constrained bubble thermo-siphon (Wayner, 1995), where surface tension and liquid affinity to the surface completely control the distribution of the liquid in the device. The low importance of gravity in the performance of the constrained bubble thermo-syphon has caused it to be considered for thermal management applications in space. This indicates that the performance of the current design for the target condensation region depends on both gravity and surface tension. The bond number normally used to scale the relative importance of surface tension into gravitational effects is given as:

$$B_o = \frac{g.(\rho - \rho_f).d^2}{\sigma} \tag{4.1}$$

where, d is the droplet/ bubble diameter in m, ρ is the droplet/bubble density in Kg/m^3,

ρ_f is the surrounding fluid density in Kg/m^3, and σ is the surface tension in N/m. The bond number for optimized target with d_c taken as 0.005 m and thermo-physical properties for water saturated at 4.7 MPa (680 psia) is 3.58.

Our optimized design has been formulated for utilization in a modified RDS-111 silver target holder, with the outer dimensions unchanged to allow utilization of a stock target holder carousel. The use of the RDS-111 target holder limited the cross sectional area available to construct target volume. It would be preferred to move the condensation volume further above the beam strike to enhance the elevation change available to drive condensate return flow. A larger target holder diameter would also allow enlargement of the cross-sectional area for steam flow in the front region of the target, where the steam volume flow moving toward the back of the condensation region is maximum. The current optimized design has a peak steam velocity of roughly 1 m/s moving toward the back of the target when operating at 1000 W power and 4.7 MPa (680 psia). This steam flow will inhibit the flow of liquid forward toward the beam strike, and poses some slight risk of limiting the claimed thermal performance per unit target mass. Further extension of the condensation region length, L_c, is precluded by excessive steam velocities in the front of the target when the RDS-111 silver target holder is used as a baseline.

Current RDS-111 target performance is not very sensitive to the heat transfer between the target holder and the process cooling water. The extension of the target power to 1,000 Watts makes the performance of the target holder heat sink more important, but it remains adequate.

CHAPTER 5. EXPERIMENTAL FACILITY DESIGN

5.1 Overview of the Facility

An experimental facility has been designed and constructed to evaluate the thermal performance of the optimized enriched water target. The facility was built in the Nuclear Engineering Department of the University of Tennessee and a photograph of the facility is shown in Fig. 5.1. Component specifications followed in industry and market are in the English system of units. For this thesis, SI units are used with English units in parenthesis. Saturated steam travels from the electric heater into the test section. The process water circulated by the metering pump condenses the steam. Gravitational force drives the condensate from the test section back to the heater. This completes one thermodynamic cycle. As the steam travels through the Main Steam Line (MSL), it passes a safety valve, a pressure gauge, a steam trap, and an air relief valve. The liquid component in the steam gets collected in the steam trap and flows through the Recirculation Line (RL) back to the heater. The gage and relief valve are set to gage pressures (i.e., $P_{gage} = P_{act} - P_{atm}$). When steam pressure exceeds 689.5 KPa (100 psig), i.e., the set pressure for the safety valve, the safety valve opens and redirects the steam from the MSL into the sink tank through the Bypass Line (BL). The other tank is used for the process water storage. This chapter will describe the design of the aforementioned components.

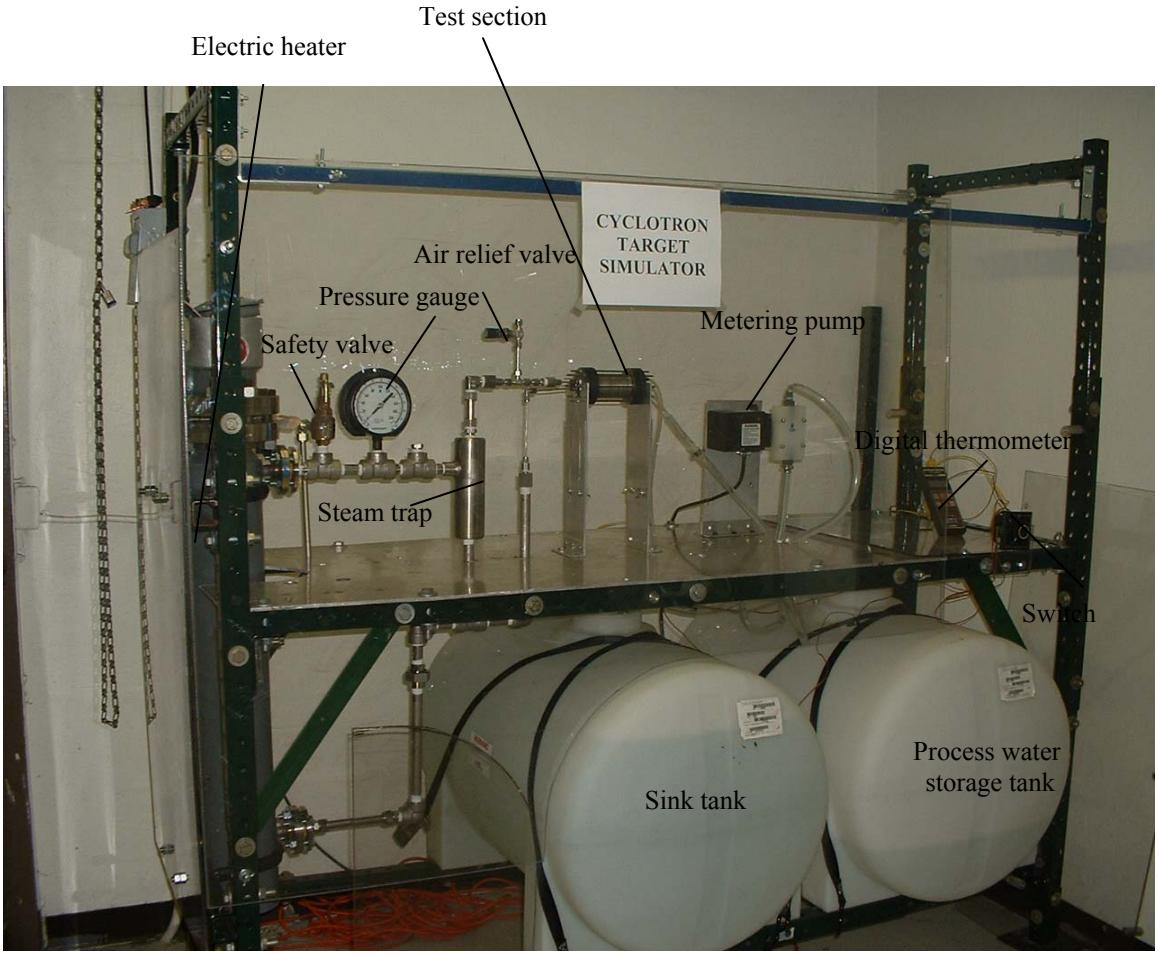

Fig. 5.1 Overview of the facility

5.2 Heater Design

An electric heater in a pressure vessel is used as the steam generator. The principal heater design parameters are the operating temperature, pressure, and power. Maximum pressure and temperature values are taken from the information provided by CTI, Inc. The value of Power was obtained from the MATLAB target thermal simulation. Extensive study of the commercially available heaters is done and a clean water re - circulation heater is selected for this purpose. Circulation heaters are designed to heat a flowing medium installed in-line or on a side-arm branch. This heater was delivered complete with built-in heating elements, heating chamber, thermostat, and insulation. The heater is shown in Fig. 5.2.

This heater is a custom-made product of Warren Electric Corporation. The components are ASME certified to operate at 4.83 KPa (700 psig) at 315.55^{o}C (600^{o}F). The heater operates in a single-phase circuit at 240 volts with a maximum power generation of 2 KW. For safe operation, the minimum immersed length of heaters is 81.28 cm (32”). The heater consists of the following elements. Three Incoloy elements are welded to two 7.62 cm (3”) x 600# ANSI type 304 stainless steel flanges. A type K thermocouple (ungrounded) is located in the thermo well. Steam temperature is controlled using a thermostat. This thermostat can operate over a range of 121.11-454.4^{o}C (250-850^{o}F). The terminal enclosure is explosion/weather resistant with two 3.81 cm (1½”) conduits. Watt density of the heater is 1.4 W/cm^{2} (9 Watts/ Sq. Inch). The casing for the heater is made of 304 stainless steel with 2.54 cm (1”) thick Calcium Silicate insulation and metal jacketed.

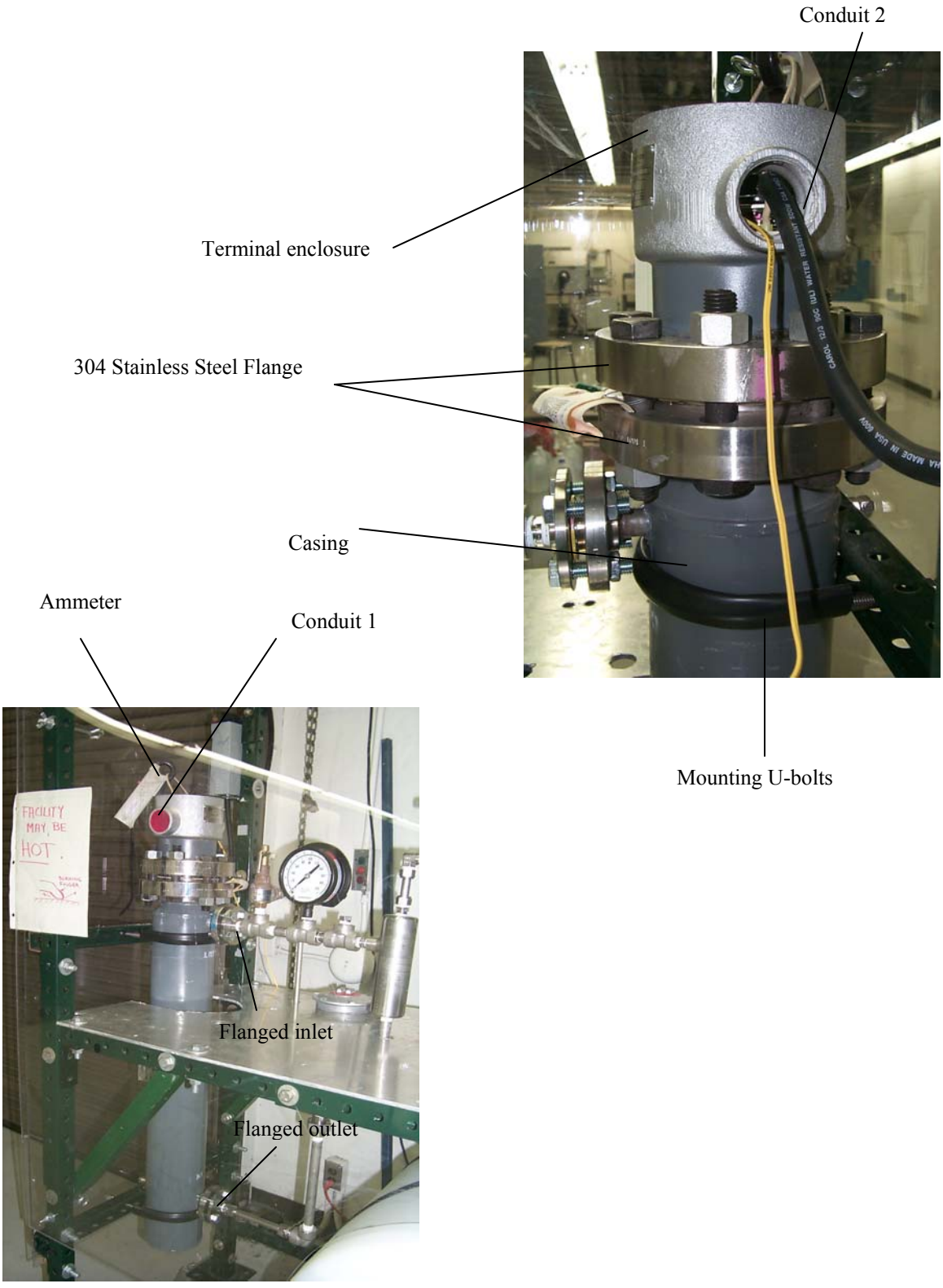

Fig. 5.2 Heater design

The heater vessel is a 7.62 cm (3”) schedule 40 SA-312 pipe with 1.27 cm (1/2”) x 600# ANSI flanged inlet and outlet. Flanged fittings are easy for assembly and disassembly. Vent and drain with plugs are provided with 1.27 (1/2”) x 3000 # NPT configuration. The heater is mounted to the experiment space frame with a set of mounting U-bolts.

5.3 Instrumentation Flange 1

The instrumentation flange 1 is shown in Fig. 5.3. and is fabricated in the UT Nuclear Engineering Department. It is a 7.62 cm (3”) flange constructed of mild steel. The 2D drawing of flange 1 is given in Fig. 5.4. This flange is located on the primary side of the facility. Eight holes of 0.43 cm (0.17”) diameter are drilled equiangular on the flange 1. Each of the eight holes accepts 8-32 threaded studs, which upon tightening with nuts seal the two flanges to the Lexan tubing and the test section. Hole 1 and hole 2 are through holes that are threaded for 0.0625 cm (1/16”) compression tube fitting. Military grade Teflon tape is used as a thread sealant between the compression tube fittings and the holes. These fittings run on the target side of the flange and are discussed later. Hole 3 is designed to accept a locating pin of 0.3 cm (0.12”) diameter. This locating pin holds the test section in position. An O-ring provides the seal between the test section and the flange. O-ring gland is machined on the target side of the flange. Design of the O-ring gland is the critical part. Static glands are desired as the test section is fixed during operation. These glands when used with an appropriate O-ring will form a leak tight seal between the test section and the flange.

Target side

Primary side

Fig. 5.3 Instrumentation flange 1

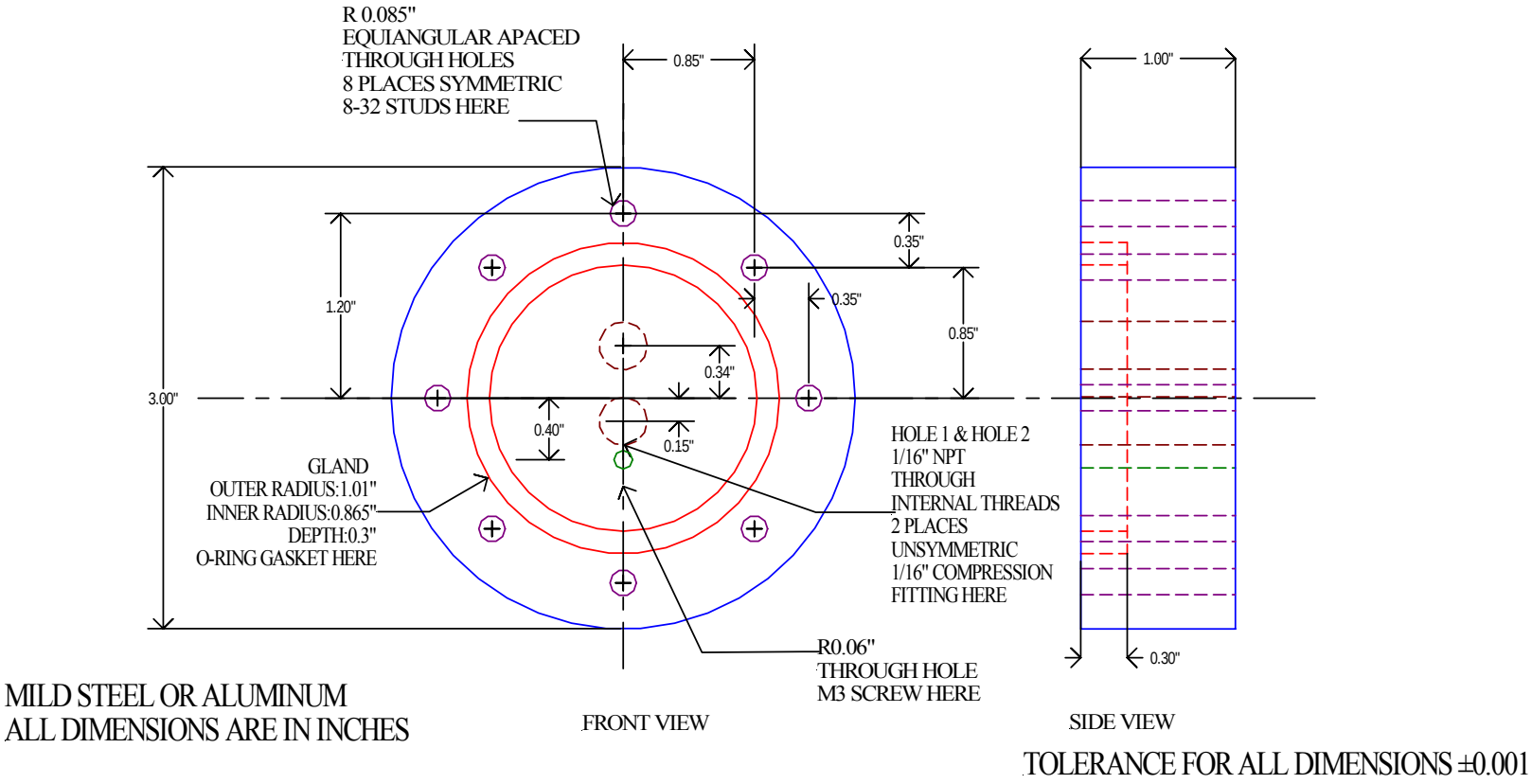

Fig. 5.4 2D drawing of instrumentation flange 1

Gland dimensions are obtained from the charts based on the O-ring chosen. O-rings are available in standard sizes. Standard sizes are set by Aerospace Standard AS568A and are designated by dash numbers. The dash number for the O-ring chosen is 224. The O-ring has an outer diameter of 5.08 cm (2”), inner diameter of 4.44 cm (1 ¾”) in., and a width of 0.3175 cm (1/8”). Inner and outer diameters of the O-ring and the Lexan tubing are equal. This black colored O-ring is made of Buna-N (Nitrile) that is widely used in many applications. These O-rings have high tensile strength and high abrasion resistance. The temperature range of this O-ring is -37.2 ^{o}C to 121.11 ^{o}C (–35^{o}F to +250^{o}F). From the standard charts for AS568A Dash No. 224, the gland width is 0.47 cm (0.187”) to 0.49 cm (0.192”), gland depth is 0.2810 cm (0.111”) to 0.29 cm (0.113”). The gland dimensions used for fabrication vary slightly from the standards. The width and depth are greater than the standard dimensions. This will facilitate the Lexan tubing to slide into the groove. Dimensions did not match due to defect in manufacturing and the design failed during the leak test. A back up ring is used and the primary O-ring is sanded such that there is zero clearance between the target section and the flange when the lexan tube is pressed against the O-ring. A small amount of silicon sealant is applied on the lexan tube edges and the O-ring surface. This was thought to be a best possible way to solve the leak problem without replacing the flange.

5.4 Instrumentation Flange 2

The instrumentation flange 2 is shown in Fig. 5.5 and its 2D drawing is shown in Fig. 5.6. This flange is located on the secondary side of the facility. Like flange 1, it has an array of eight equiangular spaced holes to accept 8-32 threaded studs, which upon

Target Side

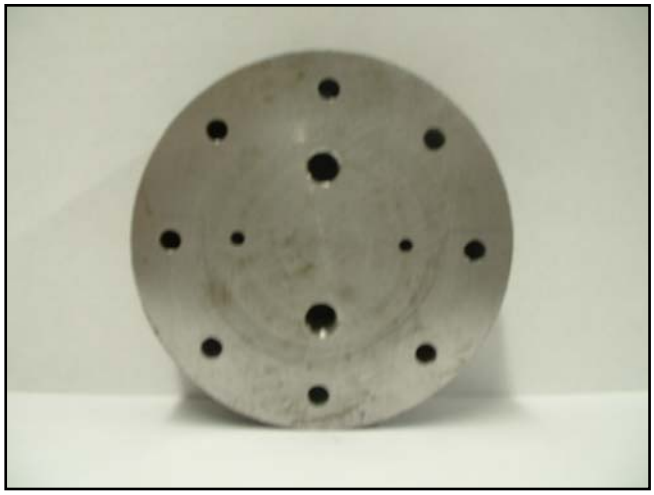

Secondary Side

Fig. 5.5 Instrumentation flange 2

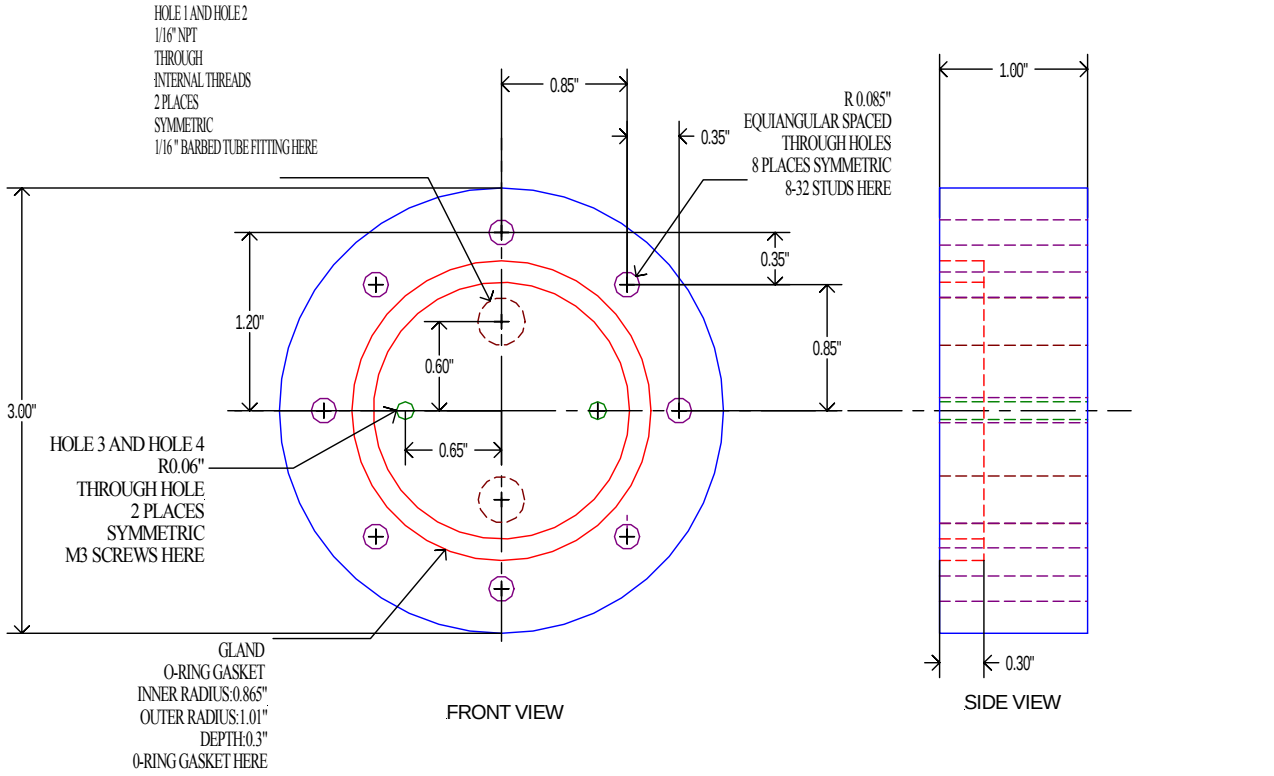

Fig. 5.6 2D drawing of instrumentation flange 2

tightening with nuts seal the two flanges to the Lexan tubing and the test section. The difference between flange 1 and flange 2 is the location of hole 1, hole 2, hole 3 and hole 4. Hole 1 and hole 2 are located on the vertical central axis. These are through holes that are threaded for 0.16 cm (1/16") nylon single-barbed tube fitting. These fittings run on the secondary side of the flange. Teflon sealant is inefficient for metal-plastic contact. Therefore, silicon sealant is applied to the barbed tube fittings and inserted in the flange. Hole 3 and hole 4 are located on the horizontal central axes that accept locating pins for the test section. Hole 3 and hole 4 were never used, hence they are closed using a tapered brass pin with silicon sealant. O-ring gland is machined on the target side of the flange. The same procedure is followed for design, manufacturing and fixing of leaks as flange 1.

5.5 Process Water Storage Tank and Sink Tank

The process water storage and sink tanks are shown in Fig. 5.7. Storage tank is used to store the process water and blowout tank is a dual-purpose tank. It stores the exit water from the test section and is the suppression tank for the high-pressure steam from the main steam line pressure relief valve. Both are high-density polyethylene tanks and the color is translucent white. The maximum operating temperature of the tank is 54.44^{o}C (130^{o} F). These tanks have molded legs and are graduated in both gallons and liters. The dimensions of the tanks are 58.42 cm (23") diameter, 97.8 cm (38 ½") overall length, 63.5 cm (25") overall height and 0.635 cm (1/4") wall thickness. The tank capacity is

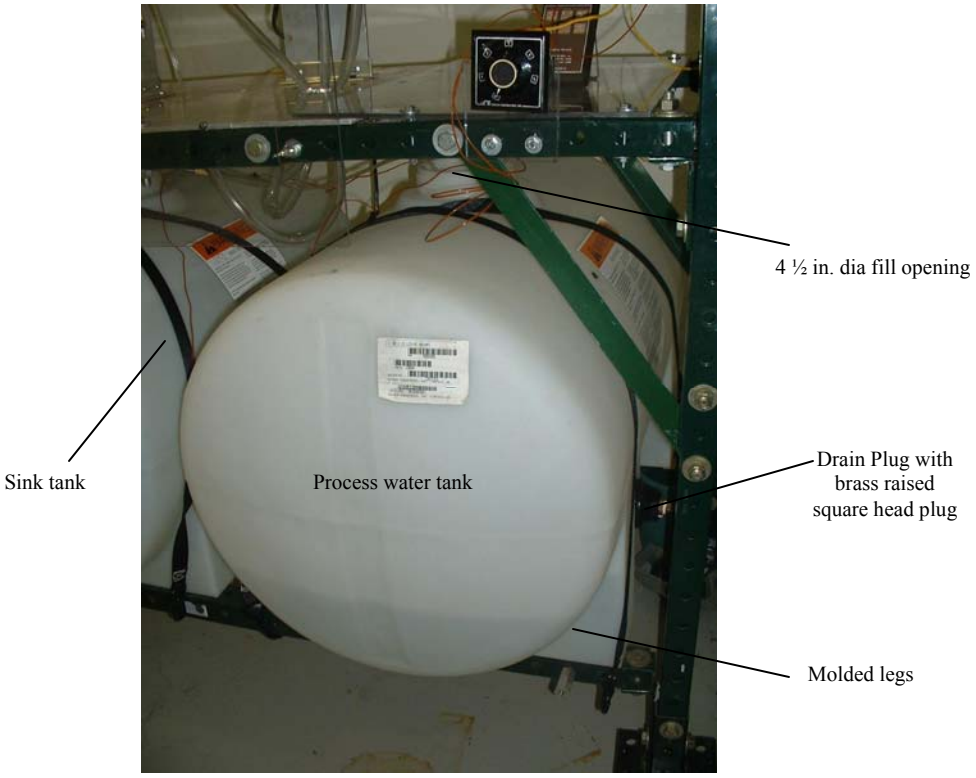

Fig. 5.7 Process water storage tank and sink tank

264.3 L (60 G) and has a threaded fill cap and an 11.43 cm (4 ½") diameter fill opening. The drain opening is located on the end of the tank and has a polyethylene, 2.54 cm (1") NPT female bulkhead fitting with a Vinyl gasket. The drain opening is closed with a 2.54 cm (1") brass raised square head plug. The function of these two tanks may be exchanged depending upon the inventory level. This can be done by interchanging the two lines from one tank to another.

5.6 Process Water Pump

Based on the data provided by CTI inc., and the data used in the computer simulation models, a pump should be acquired with a maximum flow rate of 2 L/min.

The pump flow rate should also be variable. Liquid pump selection flow chart in the Cole-Parmer catalog was used and a diaphragm metering pump was chosen for this purpose based on the design constraints. The pump is shown in Fig. 5.8. Metering pumps move precise volumes of liquid in a specified period to provide accurate flow rates. This class of pumps moves the liquid in two stages: the suction stroke and the discharge stroke. During the suction stroke, liquid is pulled into the pump cavity past the inlet check valve. During the discharge stroke, the inlet valve closes and the outlet valve opens allowing the liquid to be pushed out. The flow rate is varied by either varying the stroke length or varying the cycle frequency.

Fig. 5.8 Metering pump

The only disadvantage of this pump is the flow pulsations. To avoid this problem, the flexible delivery line is extended providing a compressible volume large enough to make the flow continuous entering the target holder. The pump maximum flow rate is 2 L/min (32.5 GPH). Flow rate can be varied through a cam type adjustment with an infinite number of settings between zero and 100% of the maximum pump capacity. The pump is 17.78 cm (7") wide, 20.32 cm (8") high and 16.51 cm (6.5") depth and the maximum operating temperature is 60^{o}C (140^{o}F).

5.7 Instrumentation and Controls

For a saturated system, pressure and temperature are the critical parameters to be measured. Saturation pressure in the main steam line is monitored using a pressure gauge. The pressure gauge is shown in Fig. 5.1 and is a product of McMASTER-CARR. This is a general service bourdon tube pressure gauge and it measures positive pressure relative to atmospheric pressure. Features of this pressure gauge include a full-scale accuracy of ± 0.5% (Grade 2A), ambient temperature range of -40°C to -101°C (-40° to +150° F) and process temperature range of -40°C to -101°C (-40°F to +250°F). The gauge has a dual scale that reads in psi and KPa and has 1.27 cm (1/2") NPT male brass connection. Readings are noted manually.

Temperatures at three locations are monitored for the current system using type K thermocouples. Saturated steam temperature (T1), Process water inlet temperature (T2) and Process water exit temperature (T3). An ammeter is hooked onto the heater wiring that measures the supply current. The system should shut down when the system

temperature equals thermostat set temperature (T_{set}). The ammeter provided confirmation of heater status. A digital thermocouple readout is used to display the temperature. The thermocouple readout has 0.1^{o} reading precision and can accept type J, K and T thermocouples. Units of ^{o}F and ^{o}C may be displayed over full range. The three thermocouples are wired to a single rotary switch and then run to the digital thermometer. By rotating the switch, the three temperatures can be recorded.

A safety relief valve is used to protect the current system from excessive steam pressures. The safety valve shown in Fig. 5.1 and is supplied by McMASTER-CARR. The pressure was factory-set for 100 psig (689.5 KPa) and is not adjustable. This valve will automatically "pop" open if the set pressure is exceeded, and remain open as long as the pressure is above this level. When the pressure level drops back to the set pressure, the valve will automatically close. This valve has a 1.27 cm (1/2”) male inlet and 1.905 cm (3/4”) female outlet. The connections are discussed later. For experiments that require operating conditions greater than 100 psig (689.5 KPa), the low-pressure pop-safety valve can be replaced with a high-pressure pop-safety valve.

5.8 Steam Trap

The steam trap is shown in Fig. 5.9. The Steam trap separates the liquid component of the steam and delivers dry steam to the test section. This is a 316 stainless steel construction with three openings as shown. Steam enters from the left side and leaves from the top. Liquid component gets collected and flows down through the pipe to return to the heater.

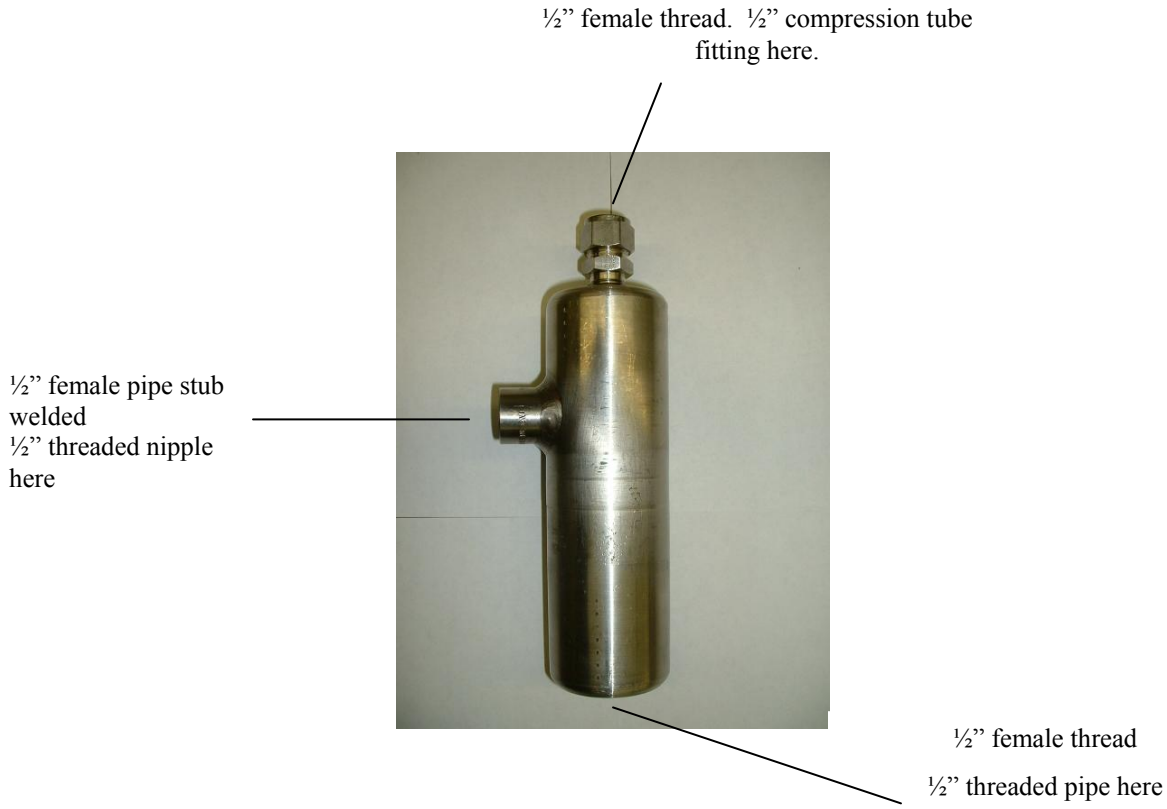

Fig. 5.9 Steam trap (units in inches)

5.9 Pipe Lines and Pipe Fittings

Three different pipelines are designed on the primary side of the current system. Line 1, Main Steam Line (MSL), is used to deliver steam from the electric heater to the test section. Line 2, Recirculation Line (RL), drives the condensate from the test section and the steam trap back to the heater. Line 3 is the Bypass Line (BPL) that drives excess pressure steam out of the heater into the blowout tank. Two different tube lines are designed on the secondary side (Process Water). The Process Water Delivery line (PWDL) delivers process water from Tank 1 to the test section. The Process Water Return line (PWRL) drives water from the test section to the return tank. The configurations of these lines are discussed below.

5.10 Main Steam Line (MSL)

The Main Steam Line (MSL) is shown in Fig. 5.10. The MSL runs from the heater to the steam trap and then takes a 90^{o} turn and runs into the test section. This is accomplished by using various pipes, pipefitting, tube and fittings. The heater vessel is a 7.62 cm (3") schedule 40 SA-312 pipe with 1.27 cm (1/2") x 600# ANSI flanged inlet and outlet. Type 316 stainless steel Cast Flange (CF) is used for the MSL. This flange is coupled with the heater flange using gasket, nuts and bolts to form a leak free fit as shown in Fig. 5.11. An 8.9 cm (3½") flange is threaded to accept a 1.27 cm (1/2") male pipe. Unlike the heater flange, this flange and gasket can withstand pressures up to 1034.2 KPa (150 psi). These parts must be replaced for operating pressures beyond 1034.2 KPa (150 psi).

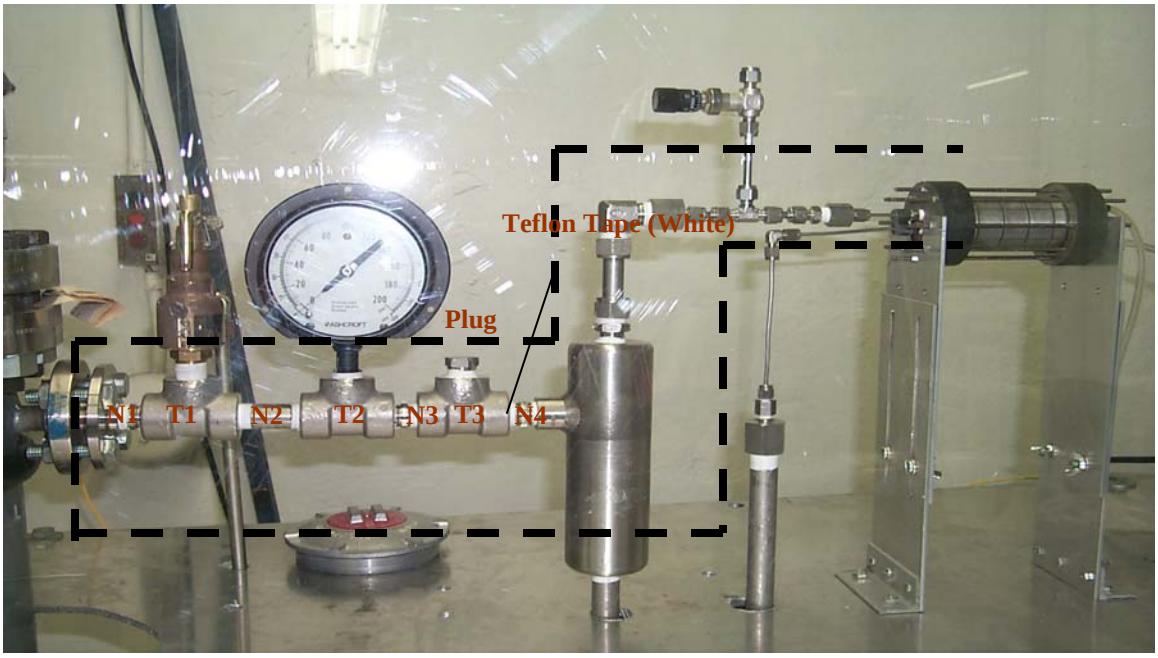

Fig. 5.10 Main Steam Line (MSL) in the dotted region

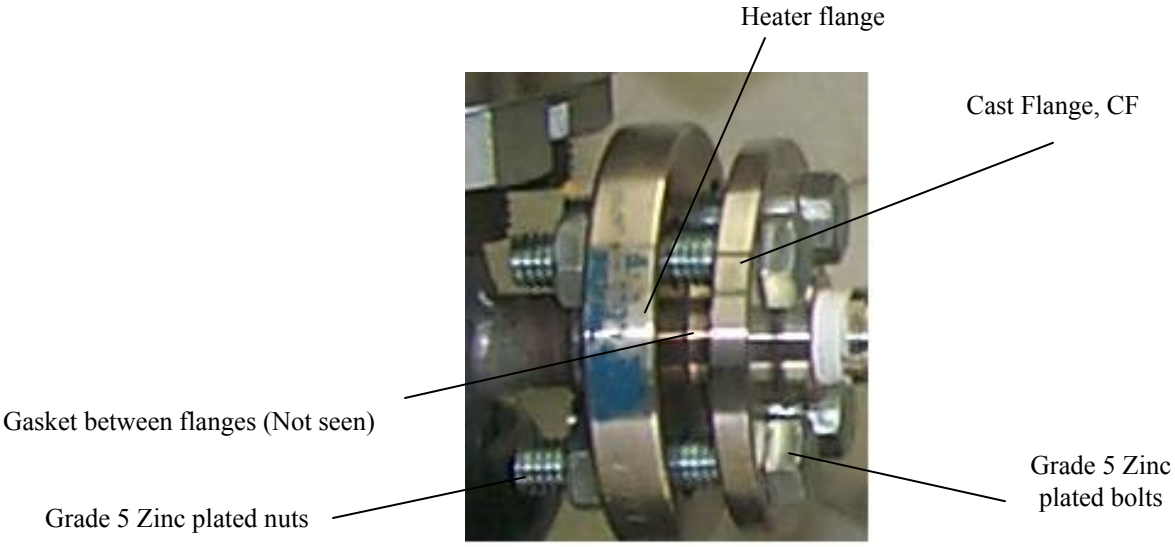

Fig. 5.11 Coupling heater flange and main steam line flange

Four nipples (N1, N2, N3 and N4) with three Tee fittings (T1, T2 and T3) are used between the flange and the steam trap as shown in Fig. 5.10. Nipples are used to have minimum line length to reduce pressure loses. N1, N3 and N4 are of same configuration. These are 1.27 cm (1/2") pipe; 3.81 cm (1 ½") long round center nipples made of 316 stainless steel and can withstand pressures up to 645.5 MPa (600 psi). N2 is chosen longer (6.35 cm) in order to provide room for the 11.43 (4 ½") pressure gauge dial. N2 is a dual rated 316/316L stainless steel welded pipe nipple. It is a schedule 40, 1.27 cm (1/2") pipe. All the Tee- fittings are made of type 316 stainless steel and can accept these 1.27 cm (1/2") threaded nipples and pipes.

These fittings can withstand pressures up to 20.7 MPa (3000 psi) and can operate at temperatures ranging between – 425^{o}C to + 1500 ^{o}C. T1 accepts N1, N2 and the Pop-Safety Valve. T2 accepts N2, N3 and pressure gauge. T3 accepts N3, N4 and a ½ in. stainless steel plug. This plug is removed to check the fill level. All these parts are assembled using Teflon tape sealant. Assembly and disassembly is difficult when threaded fittings are used.

The second part of the main steam line runs from the steam trap to the test section that is shown in Fig. 5.12. The outer diameter of the tube at the outlet of the steam trap is 1.6 cm (5/8") and is 0.32 cm (1/8") at the inlet to the target simulator. Steam line should be designed to accommodate the pressure loses due to reduction in the tube diameter and should be able to withstand high temperatures and pressures. C1 is a 316 stainless steel straight adapter with a Yor-Lok compression tube fittings for 1.6 cm (5/8") tube outer diameter and 1.27 cm (1/2") Male NPT.

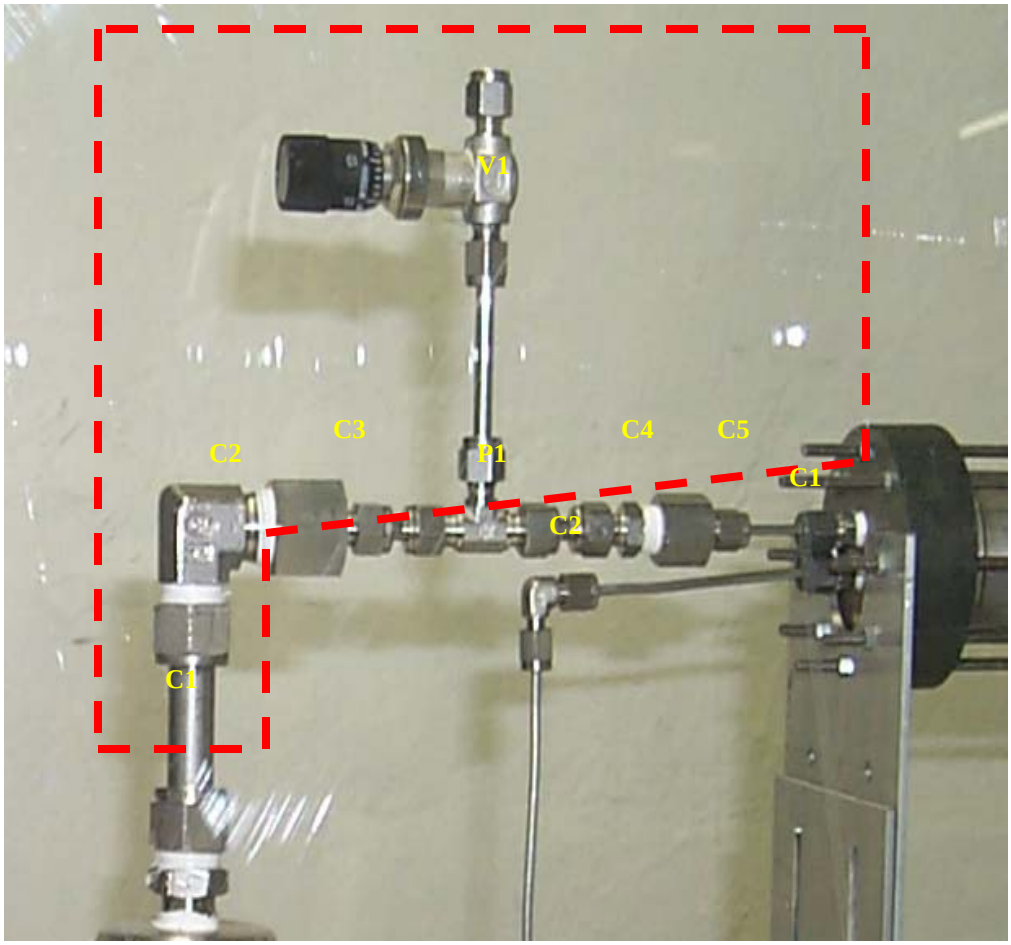

Fig. 5.12 Main Steam Line (MSL), Second Part

C2 is 316 stainless steel 90 degree elbow fitting with a Yor-Lok compression tube fitting for a 1.6 cm (5/8”) tube outer diameter and a 1.27 cm (1/2”) Male NPT. C3 is 316 stainless steel straight adapter with a Yor-Lok compression tube fitting for 0.635 cm (1/4”) tube outer diameter and a female 1.27 cm (1/2") NPT threaded fitting. P1 is a 316 stainless steel Tee fitting with a Swage-Lok compression tube fitting for 0.635 cm (1/4”) tube OD. V1 is a manually operated air relief valve built in a Tee fitting with a Swage-Lok compression tube fitting for 0.635 cm (1/4”) tube outer diameter. C4 is a 316 stainless steel male straight adapter with a Yor-Lok compression tube fitting for 0.635 cm (1/4”) tube outer diameter and 0.635 cm (1/4”) NPT. C5 is a 316 stainless steel straight adapter with a Yor-Lok Compression tube fitting for 0.32 cm (1/8”) tube outer diameter and 0.635 cm (1/4”) female NPT. The final fitting in this line is a straight adapter C5. C5 is made of 316 stainless steel. It has a Yor-Lok compression tube fitting for a 0.32 cm (1/8”) tube outer diameter and a 0.16 cm (1/16”) NPT threaded fitting. 316 stainless steel tubing of 1.6 cm (5/8”), 0.64 cm (1/4”) and 0.32 cm (1/8”) is used between fittings.

5.11 Recirculation Line (RL)

The Recirculation Line (RL) shown in Fig. 5.13 is a two branch line. One line comes from the test section and the other comes from the steam trap. The condensate in these two lines comes back to the heater by the action of gravity. The flange configuration shown is similar to that of the MSL. Stainless steel tube of 0.32 cm (1/8”) outer diameter runs from the compression tube fitting, C1 to the 0.32 cm (1/8”) 90-degree elbow compression fitting, C2. C1 is a 316 stainless steel Yor-Lok compression tube

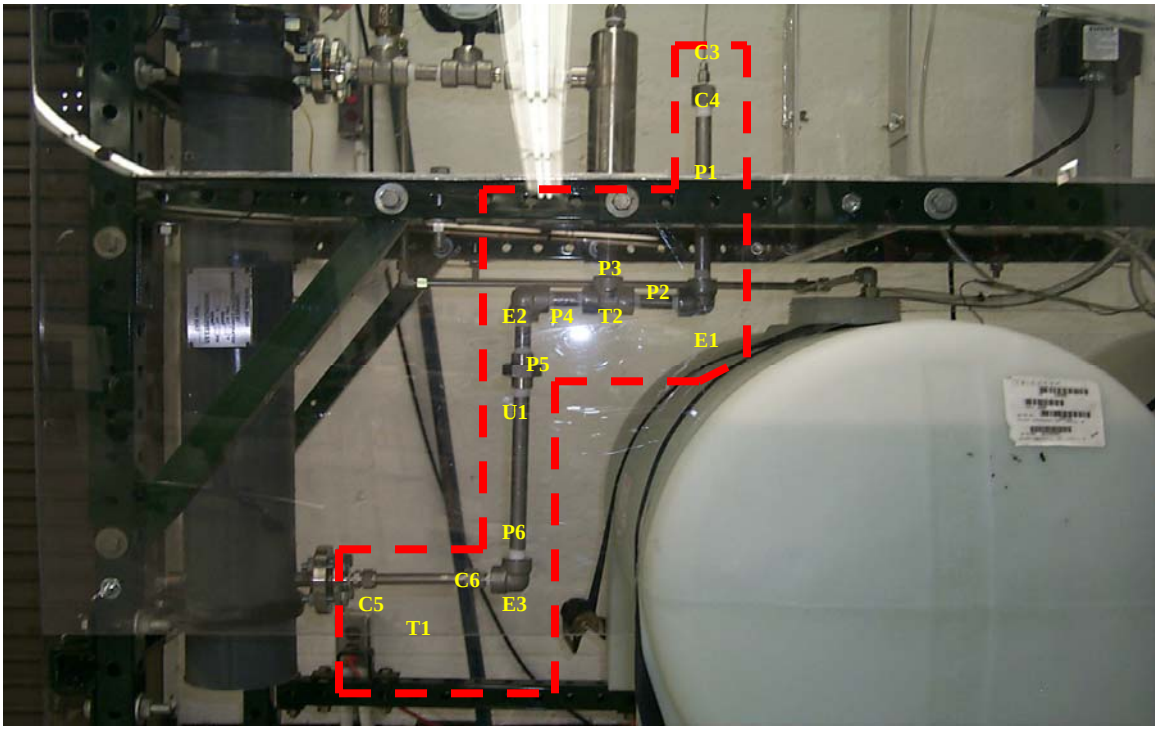

Fig. 5.13 Recirculation Line (RL)

fitting for 0.32 cm (1/8”) tube outer diameter and a male straight adapter of 0.16 cm (1/16”) NPT. C2 is a 90 degree, 316 stainless steel Swage-Lok compression tube fitting for a 0.32 cm (1/8”) tube outer diameter. C1 and C2 are shown in yellow in Fig. 5.12. C3 is a 316 stainless steel female straight adapter with a Yor-Lok compression tube fitting for 0.32 cm (1/8”) tube outer diameter and 0.32 cm (1/8”) FNPT. C4 is a high-pressure 41.37 MPa (6000 psi) adapter made of 316 stainless steel with 1.27 cm (1/2”) female x 0.32 cm (1/8”) male threaded fittings. C5 and C6 are 316 stainless steel male straight adapter with Yor-Lok compression tube fittings for 1.6 cm (5/8”) tube outer iameter and 1.27 cm (1/2”) NPT. P1, P2, P3, P4, P5 and P6 are pipes of different lengths.

These are 1.27 cm (1/2") Schedule 40 welded pipe nipples made of 316/316L stainless steel pipe. T1 is a type 304 stainless steel welded tubing of 1.6 cm (5/8") outer diameter, 1.5 cm (0.585") inner diameter and 0.05 cm (0.020") wall thickness. E1, E2 and E3 are 90-degree elbow type fittings.

These are 1.27 cm (1/2") threaded pipe fittings made of 316 stainless steel and can withstand pressures up to 20.7 MPa (3000 psi). T2 is a Tee shaped 1.27 cm (1/2") threaded pipe fitting. It is made of 316 stainless steel and can withstand pressure up to 20.7 MPa (3000 psi). The final fitting in this recirculation line is the union fitting, U1. U1 is a 316 stainless steel, 1.27 cm (1/2"). Threaded pipe with a maximum operating pressure of 20.7 MPa (3000 psi).

5.12 Bypass Line (BL)

The Bypass Line (BL) is shown in Fig. 5.14. Stainless steel is not used for the tubing and fittings since this line will not be in continuous operation. C1 is a straight adapter made of steel. It has a Yor-Lok compression tube fitting for a tube of outer diameter 1.27 cm (1/2") and a 1.9 cm (1/2") male NPT. C2, C3, C4 and C5 are 90-degree steel elbow fittings with Yor-Lok compression tube fittings for 1.27 cm (1/2") outer diameter tube. Corrosion resistant carbon steel tubing is used. This seamless tubing is an economical alternative to stainless steel. It is coated with a thin layer of yellow zinc dichromate for additional corrosion resistance.

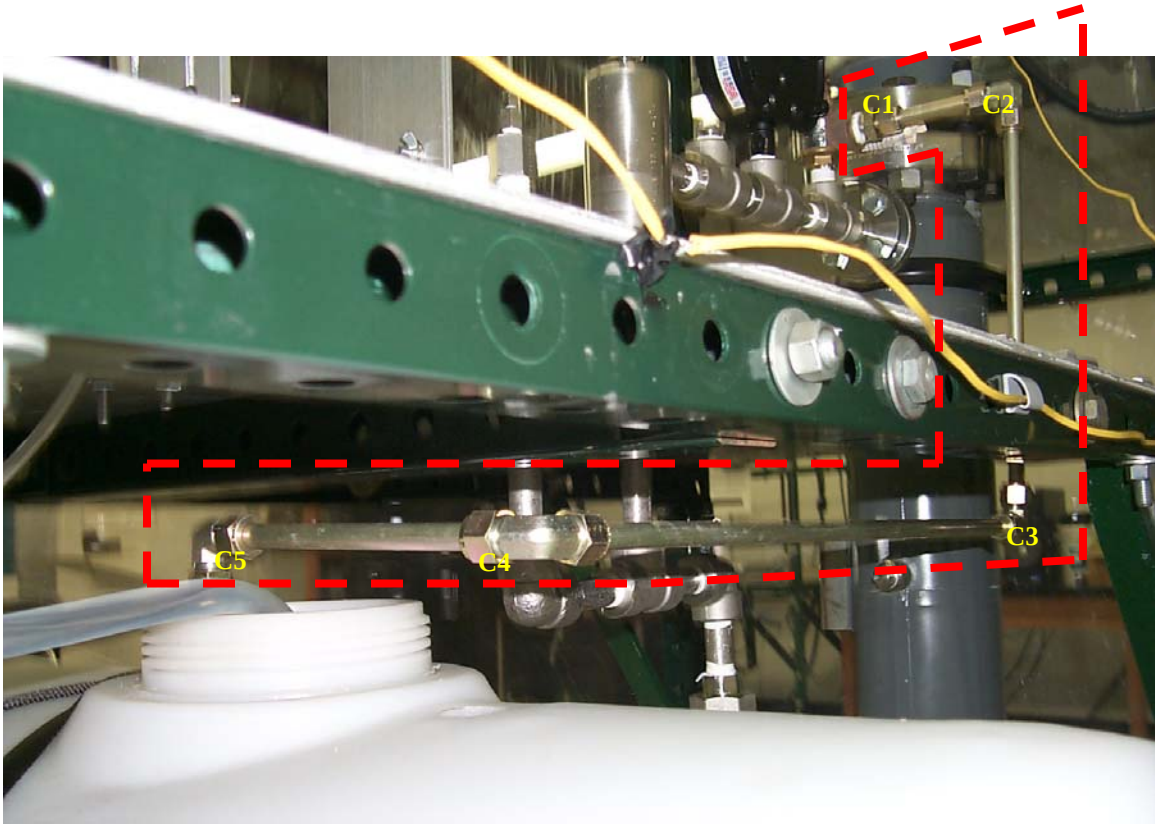

Figure 5.14 By Pass Line (BL)

5.13 Process Water Delivery Line (PWDL)

The Process Water Delivery Line (PWDL) is shown in Fig. 5.15. PWDL has 1.6 cm (5/8”) outer diameter and 1.27 cm (1/2”) inner diameter vinyl suction tubing. The vinyl suction tube is cut so that it will hang vertically 5 to 7.62 cm from the bottom of the process water storage tank. This end is connected to a foot strainer that provides filtration. The other end of this tube is connected to the intake (bottom) fitting on the pump head. The delivery side (top) of the pump is connected to the target section using three PVC tubes of different inner diameters D1 = 1.27 cm (1/2”), D2 = 0.635 cm (1/4”), and D3= 0.32 cm (1/8”). Nylon reducing couplings C1 and C2 that have single barbed

Fig. 5.15 Process Water Delivery and Return Line (PWDL & PWRL)

tube fittings achieve the reduction in diameters. C1 reduces 1.27 cm (1/2") inner diameter tube to 0.635 cm (1/4"). C2 reduces 1.27 cm (1/2") inner diameter tube to 0.635 cm (1/4"). C3 is a black colored nylon fitting with a single-barbed fitting for 0.635 cm (1/4") outer diameter tube and 0.16 cm (1/16") male NPT. Thermocouple (TC1) is inserted in-line in the suction line and silicon sealant is applied around it to avoid air and water leaks. Air leaking into the delivery line can disrupt the heat transfer. Uncertainty in the temperature measurements due to water stratification is avoided using this in-line thermocouple design. Continuous flow using a diaphragm-metering pump can be achieved using a longer delivery line that is employed in this design.

5.14 Process Water Return Line (PWRL)

PWRL is a simple design and is shown in Fig. 5.16. PVC tube of 0.635 cm. (1/4") inner diameter runs into the sink tank. Like PWDL, Thermocouple (TC2) is inserted in-line in the return line and silicon sealant is applied around it to avoid air and water leaks and is shown in Fig. 5.16. C4 is similar to C3 in PWDL. PWRL is similar to PWDL except that the water returns to the sink without any motor. The folds in the line may be better designed with clamping units.

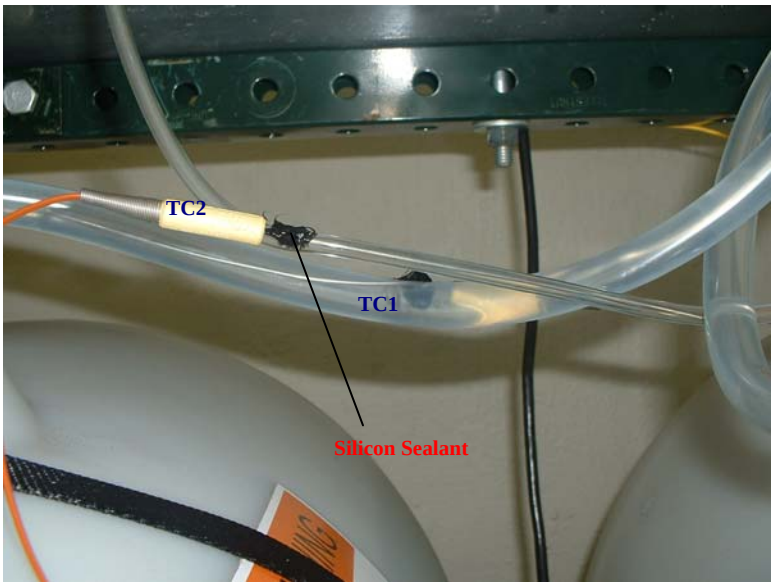

Fig. 5.16 In-line thermocouples in PWDL and PWRL

5.15 Supporting Hardware

The test section assembly has supporting hardware as discussed below. The main steam line has various fittings that cause pressure loss. From the calculations at saturation pressure of 689 KPa (100 psia) and target power of 500 Watts, the minimum pressure loss for the current system is 15.24 cm (6”). Head loss is different for different powers. To compensate the head loss, the elevation of the target section can be varied at different powers. This motivated in design of a 2-piece mounting plate as shown in Fig. 5.17. The two mounting plates are identical. This part is made from 0.32 cm (1/8”) Aluminum sheet and is fabricated in the UT Nuclear Engineering Department.

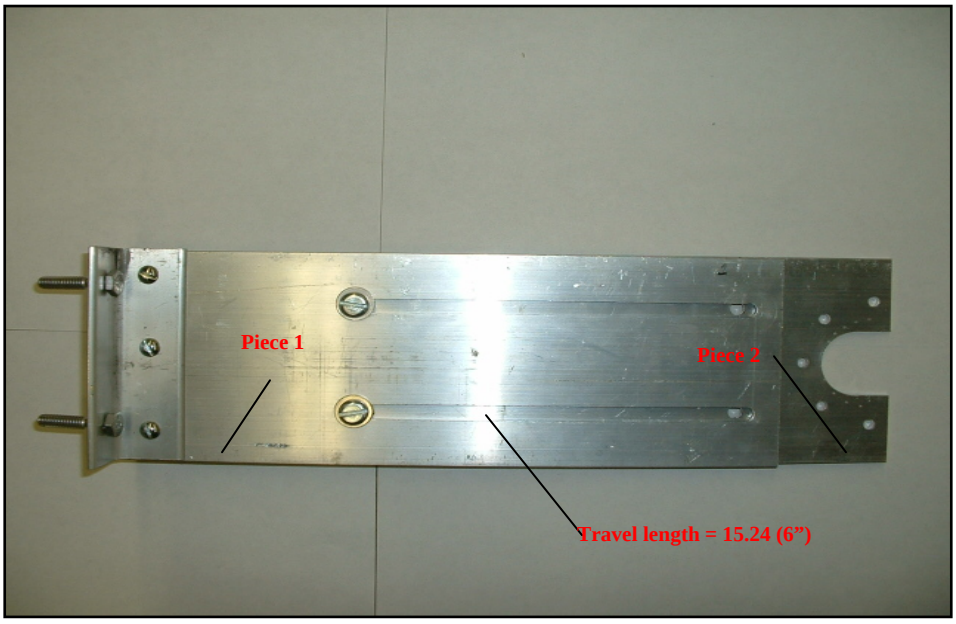

Fig. 5.17 Two-Piece mounting plate

Travel length of piece 2 in piece 1 is 15.24 cm (6”). Length is adjustable according to the pressure head loss for a particular Power, allowing compensation for the head loss. 0.32 cm (1/8”) angle aluminum is used mount these plates on the experimental platform. The semi-ellipse shape cut in the plate 1 will accommodate flange 1 and flange 2 instrumentation. Five holes are drilled around the cut to accommodate the threaded studs of the test section.

5.16 Test Section: Design and Fabrication

Aluminum (k= 200 W/(m^{o}C)) target holder was used instead of Silver (k= 400 W/(m^{o}C). This change was made because aluminum is more economical for testing. In addition, since Aluminum is a high conductivity material and the fin model remains applicable. The same software that was used for silver target volume can be used for the Aluminum target holder. CTI’s gas target holder external diameter, which is 1.5 times larger than RDS 111 target, was used for the experimental test section. This scaling was done to accommodate the steam delivery and return flow lines and planned instrumentation that is discussed in chapter 5.3 and chapter 5.4. The target cavity geometry was retained but the dimensions were scaled up by a factor of 1.5. The cooling channels on the external surface of the target holder were redesigned.

There was an increase in the external heat transfer coefficient and the new heat transfer coefficient was approximately 15,000 W/(m^{2o}C). Software was run with the new dimensions and the new heat transfer coefficient. The target power at 4.68 MPa (680 psia) was roughly 1,850 Watts. One problem that re-evaluation is the process water

cooling channel design. These cooling channels will produce non-uniform flow on the outside of the target holder that results in uneven heat transfer coefficient along the length of the fin, with the best heat transfer at the end farthest from the target. This makes the fin models with uniform external heat transfer coefficient used in the software less appropriate. The software must be modified to allow accurate comparison of simulation results with the experimental results. The test section is shown in Fig. 5.18 and the 2D drawing is shown in Fig. 5.19 and Fig. 5.20. The complexity of the target cavity made it difficult to fabricate at Nuclear Engineering machine shop. The test section was fabricated at Machined Products, Knoxville. The complicated target cavity was machined using a special machining process called Electrical Discharge Machining (EDM).

EDM is one of the most accurate manufacturing processes available for creating complex or simple shapes and geometries [2], EDM manufacturing is a very desirable manufacturing process when low parts counts or high accuracy is required. It is also used when fabrication with traditional milling operations is difficult. EDM works by eroding material in the path of electrical discharges that forms an arc between an electrode tool and the work piece. Wire EDM was used to fabricate the test section in the following way. EDM system consists of a shaped tool, a wire, and the Aluminum stock that is the work piece. The stock is connected to a power supply. To create a potential difference between the work piece and tool, the work piece is immersed in a dielectric (electrically non- conducting) fluid, which is circulated to flush away debris.

[2] Source: http://www.engineersedge.com/

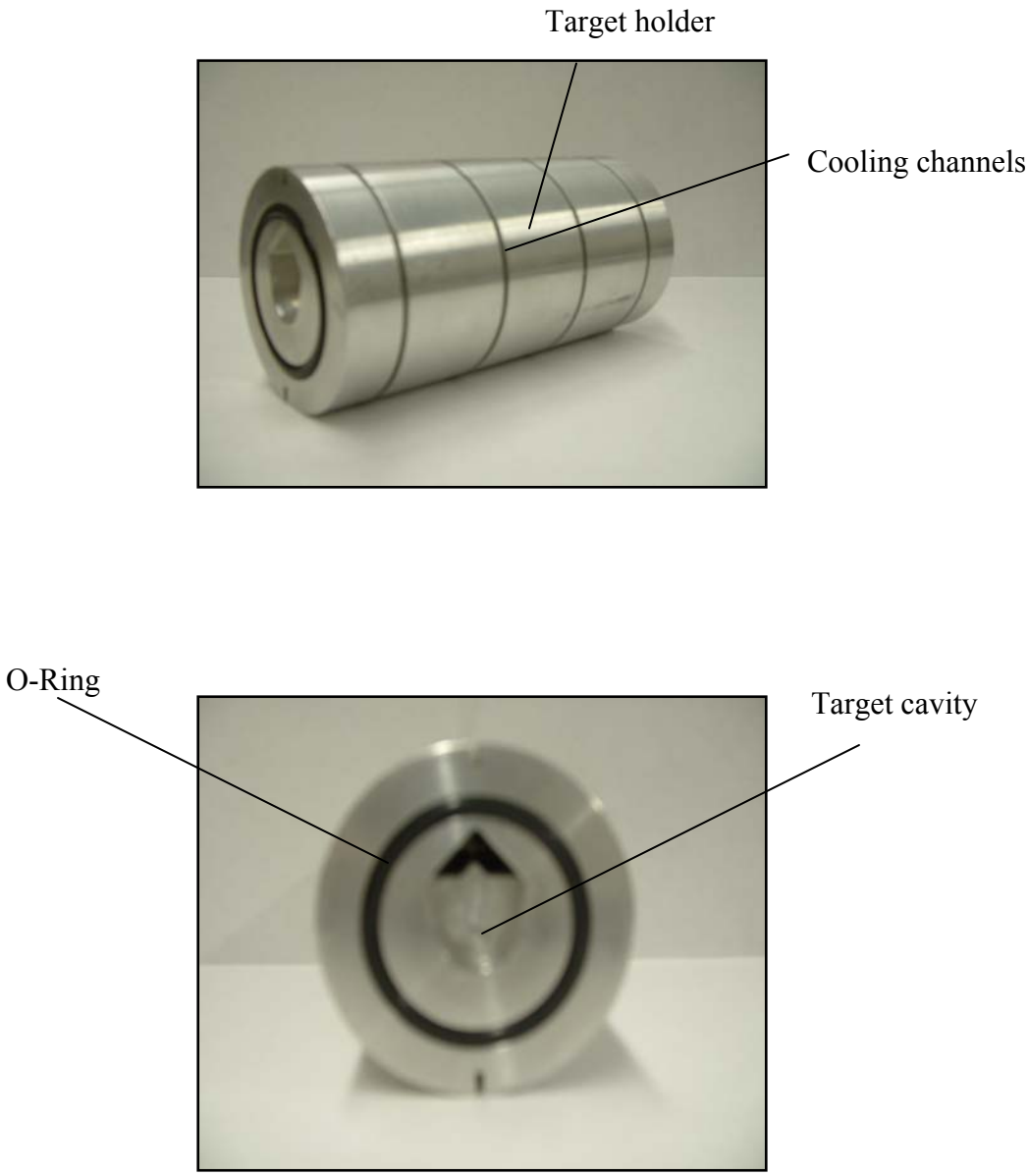

Fig. 5.18 Fabricated test section

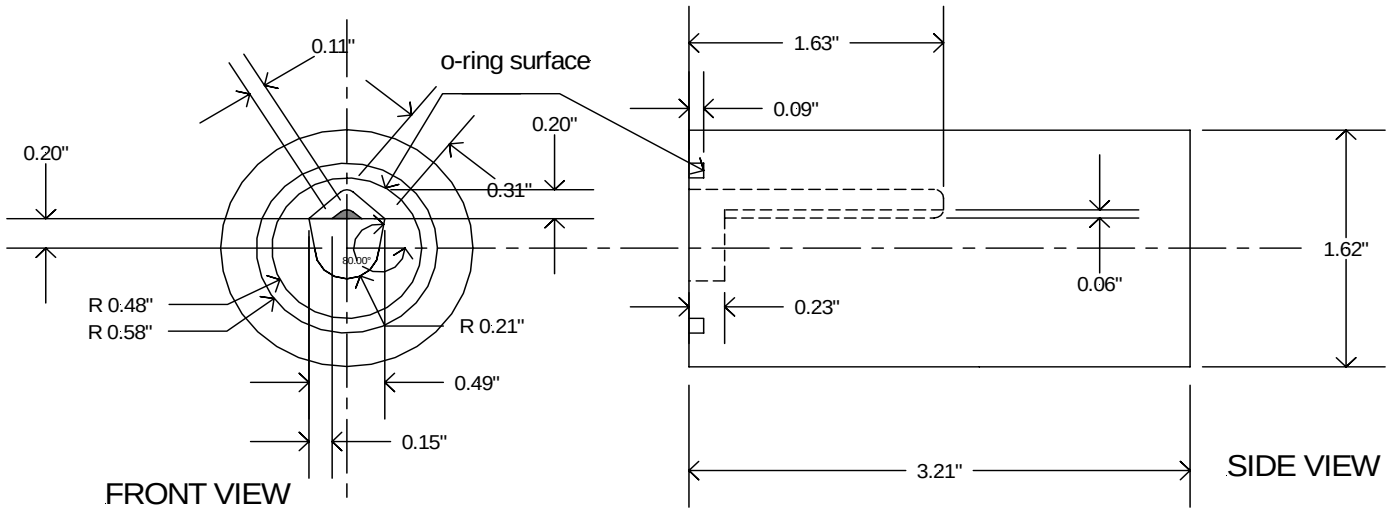

ALL SHARP EDGES ARE ROUNDED

SOLID TRIANGULAR PORTION

BELOW THE CENTER LINE :SEMICURCULAR CAVITY R 0.21", DEPTH=0.23"
ABOVE THE CENTER LINE:
TILL 0.23" DEPTH:
HALF DIAMOND SHAPE CAVITY
BEYOND 0.23 " TILL 1.63" DEPTH:
TRIANGULAR CAVITY WITH SOLID TRIANGULAR PROJECTION

Fig. 5.19 2D Drawing of the target cavity

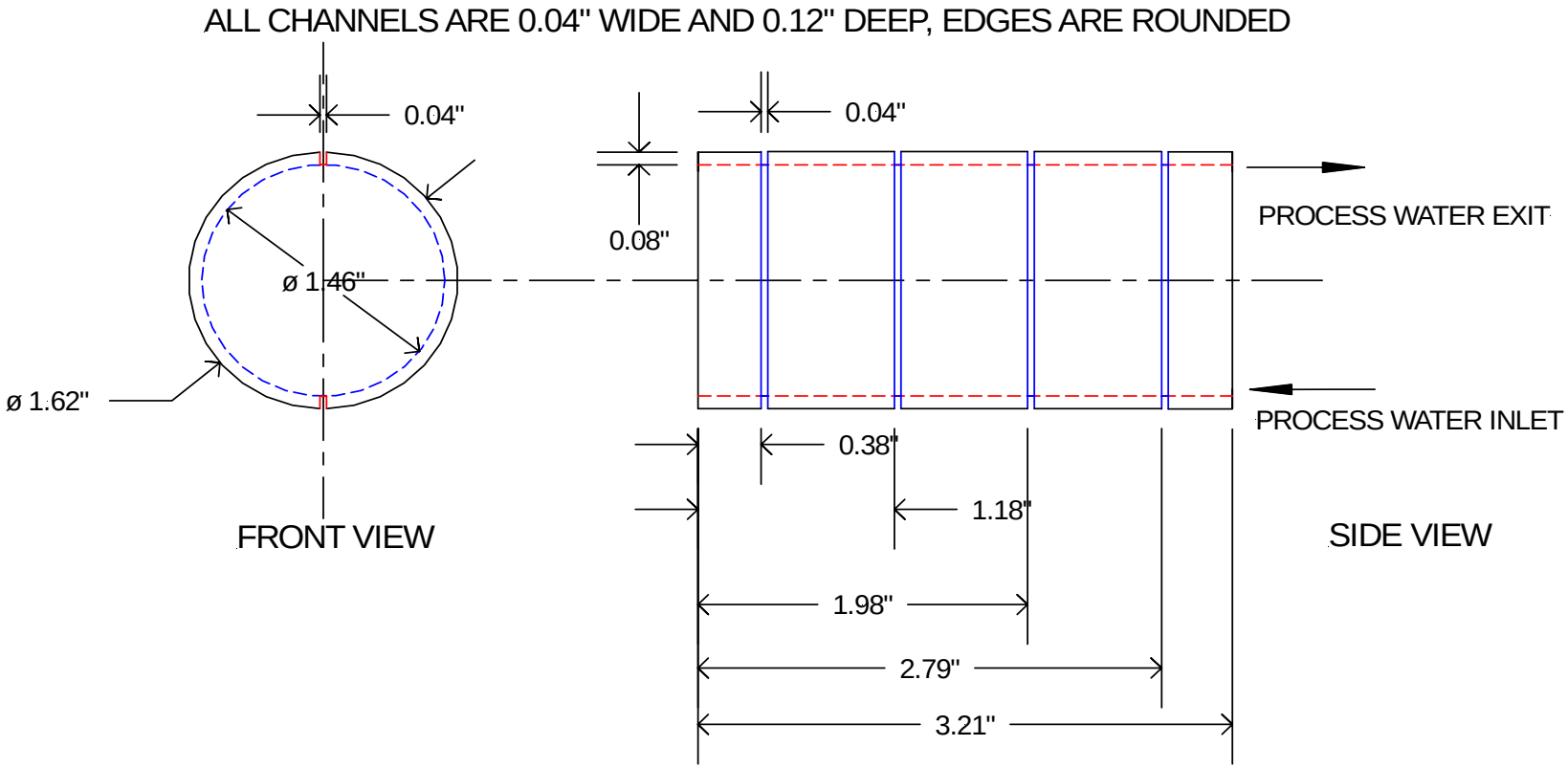

Fig. 5.20 2D Drawing of cooling channels

An initial hole was drilled in the material. Then the wire was fed through the hole to complete the machining. The cutting pattern is usually CNC controlled. The cavity was cut through the length of the target holder cylinder and the cross-section of the condensation dome was removed. The removed stock was cut to the required length and was inserted from the rear of the target holder and welded. This formed the half diamond shaped cavity with the ridge running parallel to the axis. This is the condensation dome. The semicircular shaped region and the cooling channels were fabricated with a conventional milling machine.

CHAPTER 6. STARTUP AND OPERATING EXPERIENCE

6.1 Startup Experience

The first problem observed at startup was leaks. The main steam line, re-circulation line and the two tanks were filled with water and left idle for a day to check for leaks. There were no leaks observed from the tanks. Minor leaks from the pipe lines were observed. These are due to improper tightening of the fittings that are fixed later.

Electric heater was another source of start-up problem. The electric heater was initially wired improperly and the electrical fuse was blown. Electrical connections were reworked and the heater worked properly. The supply voltage is 209 Volts coming from two legs of three-phase supply. The ammeter shows eight Amps at this voltage, placing the total heater power as 1,672 Watts. The heater is not operating at its maximum power, 2,000 Watts. This is not a major issue for predicting the target heat sink performance. Therefore, nothing has been done to increase the supply voltage.

A test was carried out to check the delivery rate of the pump. Pump was started with the target drain line open into a burette. The capacity of the burette is 1 liter. The pump was set to a certain flow rate and multiple readings were taken over a period of one minute. It was observed that the flow was very intermittent. A longer delivery line to the target from the pump was installed to add compressibility. This allows uniform delivery pressure to the target, and uniform target drain flow. The other challenges at the start up were minor problems like wiring of thermocouples.

6.2 Operating Experience

Water started leaking from the heater through the drain plugs. This happened while pressurizing the heater that resulted in the loss of inventory. The system was shut down and the total inventory was drained. The problem was rectified by applying thread sealant to the plugs and tightening them back to the position and by refilling the system.

Steam leaked from the straight adapter and the elbow adapter running from the steam trap. This is also rectified simply by tightening the fittings. Tee fitting was used as a vent that is not described in chapter 5. The plug to the fitting was opened and closed whenever it was needed. When the system was hot, this led to operational difficulty and safety concerns. Therefore, this design was replaced by a relief value that directs non-condensable gases, steam, and excess water out of the MSL. The valve is manually operated. The metering pump produced continuous noise that has been attributed to the piston movement. This is not a problem for the test facility. The facility set-up before operation is given in Fig. 6.1.

Fig. 6.1 Facility set-up before operation

CHAPTER 7. TEST OPERATIONS

Test operations were initiated by filling the process water storage tank with tap water and the Main Steam Line (MSL) and Recirculation Line (RCL) with distilled water. Thermostat is set to the desired temperature and power supply is switched ON. During the warm up cycle, vents are opened to drive non-condensable gases out of the MSL. System is closed at saturation pressure at one atmosphere and the metering pump is switched ON. Three different tests are performed at different saturation pressures and process water flow rates. Test 1 was conducted with process water flow rate set to 1.23 L/min with the power supply ON and gauge pressure varying from 0-137.9 KPa (0 - 20 psig). The flow rate was reduced to 1.01 L/min with the power supply OFF and gauge pressure varying from 137.9-0 KPa (20-0 psig). Test 2 was conducted with process water flow rate set to 1.23 L/min and gauge pressure varying from 0-344.75 KPa (0- 50 psig) when the power supply is ON and 344.75-0 KPa (50-0 psig) when the power supply is OFF. The system pressurization/warm-up rate is approximately 6.89 KPa/min with power ON, corresponding to a change in saturation temperature of 0.3– 0.5^{o}C per minute, the cool down rate is somewhat faster. Test 3 was conducted with process water flow rate set to 0.7 L/min and gauge pressure varying from 0-551.6 KPa (0-80 psig) when the power supply is ON and 551.6-0 KPa (80-0 psig) when the power supply is OFF. These results are presented and discussed in the following section.

7.1 Uncertainty Analysis

The accuracy with which data are acquired must be properly quantified. The primary purpose of the experiment is to determine the test section heat sink performance. The heat sink performance is measured in terms of the power absorbed by the process water. The Power absorbed by the process water is given by

$$q = m \cdot c_{P} \, (T_{exit} - T_{inlet}) \tag{7.1}$$

where, q is the energy absorbed by the process water, m is the mass flow rate, c_p is the specific heat of water, T_{exit} is the process water exit temperature, and T_{inlet} is the process water inlet temperature. An uncertainty analysis is performed to evaluate the accuracy of the power calculated from measured data. The mathematics of uncertainty analysis is based on the statistical treatment of error. The possible errors in each measurement are assumed to be normally distributed. The error in each measurement is assumed independent of the error in any other measurement, and the error in every measurement is described at the same confidence level. Of the statistical methods that exist to establish the error in data, propagation of error theory is often used. Suppose that quantity A is determined from quantities B and C. If B and C are independent, the uncertainty in A given by propagation of error theory is

$$\sigma A = \sqrt{\left(\frac{\partial A}{\partial B}\right)^{2} \sigma B^{2} + \left(\frac{\partial A}{\partial C}\right)^{2} \sigma C^{2}} \tag{7.2}$$

where, σB *and* σC are the uncertainties known for quantities B and C. For this test, the more practical way of obtaining uncertainty is to utilize the definition of the total derivative. The power expressed above is a function of primary variables obtained directly from the experiment. Suppose that the quantity A is expressed as a function of the independent variables C and D. Then, σA can be expressed via the total derivative as

$$\sigma A = \left(\frac{\partial A}{\partial C}\right)\sigma C + \left(\frac{\partial A}{\partial D}\right)\sigma D \tag{7.3}$$

The derivatives can be obtained either analytically or numerically. $\frac{\partial A}{\partial C}$ is the limit of the change in A divided by the change in C as the change is C approaches zero. For calculating σ q, a small perturbation can be inserted into each of the primary variables. The derivatives are then calculated by dividing the change in q resulting from the perturbation by the perturbation. From the above formula, if the perturbation of C is the uncertainty associated with C, then the term $\left(\frac{\partial A}{\partial C}\right)\sigma C$ is simply the change in A. This means that uncertainty associated with the power is the sum of the changes in q when the value of each of the primary variables is increased by its uncertainty. Since the true value of the primary variable may be the recorded value plus or minus its uncertainty, the absolute value of each change in q must be taken before summing the changes. Excel sheets are created to compute the uncertainties.

To evaluate the significance of each contributor to the uncertainty of the power, nine case studies were undertaken. The first case study discussed below is for the process water flow rate of 0.7 L/min. The first primary variable that factors into the

calculated power is the mass flow rate of the water. Before the experiments have started, the metering pump was calibrated using a burette. The pump was set to the desired flow rate and three readings are noted down over a period of one minute. For each flow rate the error associated with each reading was 0.01 L/min. For this case, the uncertainty is 1.4 %. Increasing the flow rate by the uncertainty changes the process water power from 224 Watts to 227 Watts. There is a net change of 3 Watts or 1.4%.

The next primary variable is the thermocouple temperature difference. When the system is at room temperature, thermocouple readings showed a difference of $0.1^{o}C$ so the temperature uncertainty is $0.2^{o}C$ considering reading variation on the higher and lower side. This comparison of readings was repeated in an ice bath, with the same result. For this case study, the measured temperature difference is $4.6^{o}C$. Increasing the temperature difference by 4.3 % changes the process water power from 224 Watts to 233 Watts. There is a net change of 9 Watts or 4.3 %. Thus, the temperature difference and the process water flow rate introduce error. Only two variables affect the uncertainty of the power. For this case study, the process water power is 224 ± 12 Watts. To establish error bars on the power data for 0.7 L/min, two more case studies were analyzed in the same manner but for different gauge pressures of 275.8 KPa (40 psig) and 551.6 KPa (80 psig). These results are given in table 7.1. The case studies with error bars are shown in Fig. 7.1. The figures plotted only show the heat up state. Eight other cases are studied and the corresponding data is presented in Fig. 7.2 and Fig. 7.3.

Table 7.1 Summary of case studies for uncertainty analysis

External heat transfer coefficient ($W/(m^{2o}C)$)	Gauge pressures for different cases (KPa)	Uncertainty in dT (^oC)	% Uncertainty in dT	Uncertainty in m (L/min)	% Uncertainty in m	Process Water Power (Watts)
8,446	0	0.2	4.3%	0.01	1.43 %	224 ± 12
	275.8	0.2	2.89%	0.01	1.43 %	337 ± 15
	551.6	0.2	2.98%	0.01	1.43 %	327 ± 15
11,330	0	0.2	16.66%	0.01	1.00 %	84 ± 15
	55.1	0.2	5.4%	0.01	1.00 %	260 ± 15
	110.3	0.2	4.24%	0.01	1.00 %	330±16
13,290	0	0.2	8.33%	0.01	0.81 %	206 ± 18
	165.48	0.2	3.62%	0.01	0.81 %	471 ± 20
	344.75	0.2	3.44%	0.01	0.81%	497 ± 20

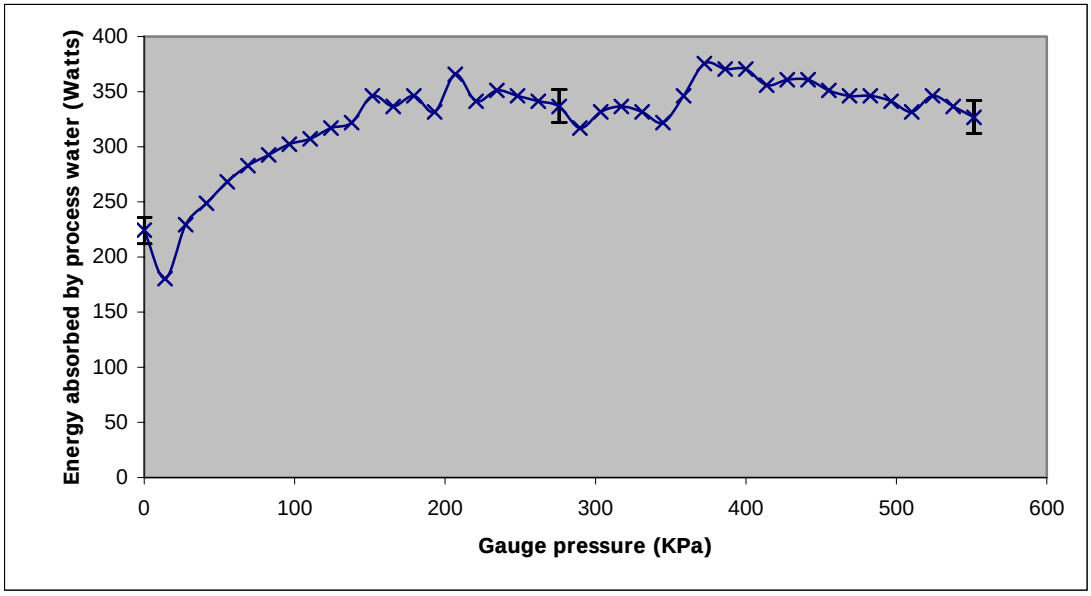

Fig. 7.1 Process water power data with error bars for h = 8,446 W/(m^{2o}C)

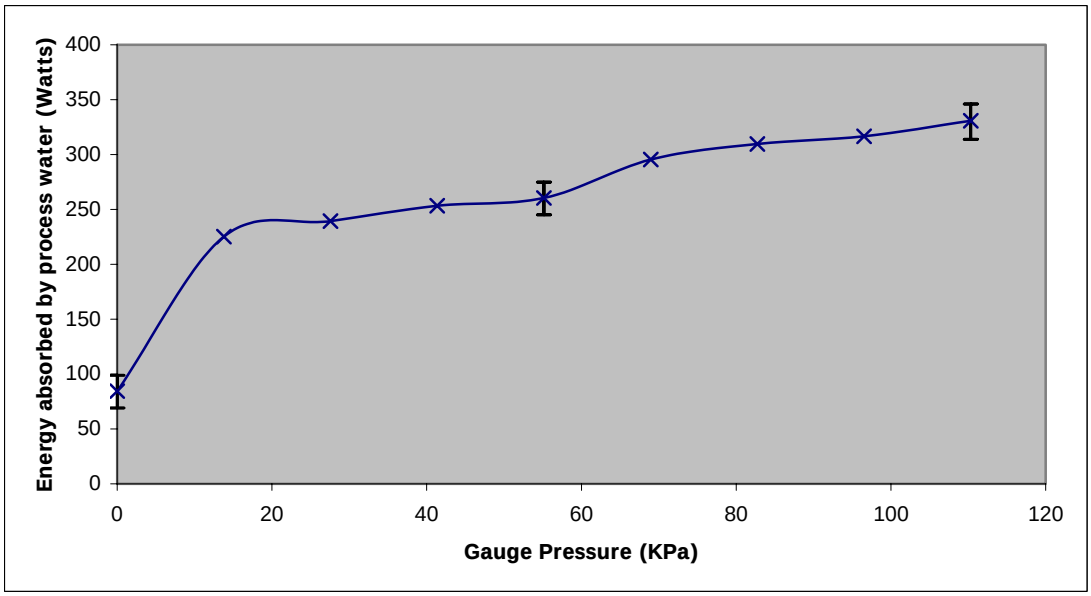

Fig. 7.2 Process water power data with error bars for h = 11,330 W/(m^{2o}C)

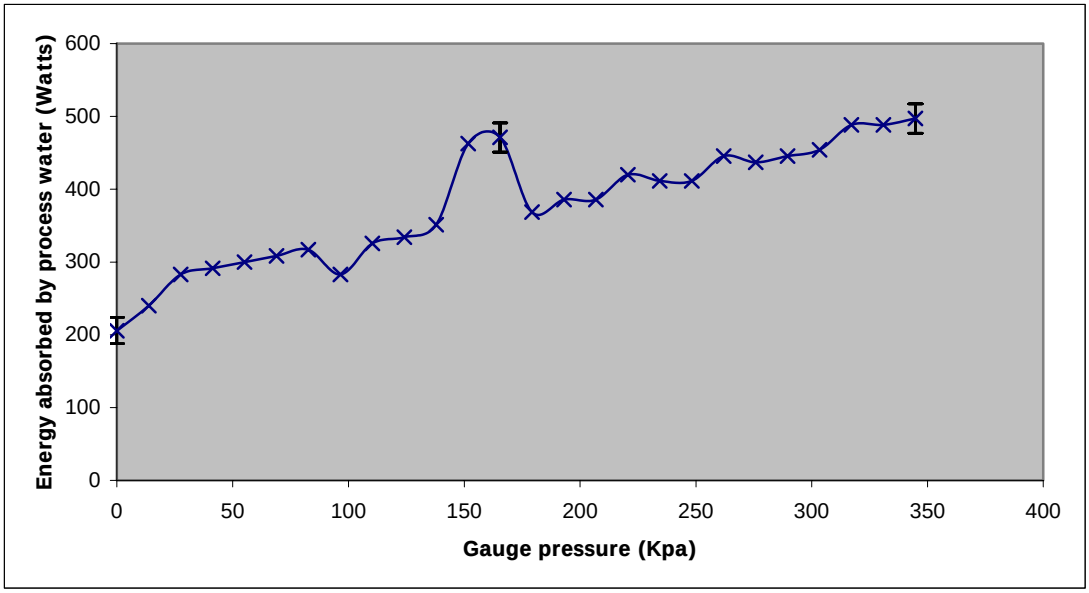

Fig. 7.3 Process water power data with error bars for h = 13,290 W/(m^{2o}C)

7.2 Energy Balance Evaluation and Analysis

Heat sink performance of the test section (target holder) was studied by varying the operating conditions on the primary and secondary sides. The primary side saturation pressure is varied by altering the saturation temperature using the heater thermostat control. Process water flow rate is varied on the secondary side by manually altering the pump stroke amplitude. Heat transferred from the target holder to the process water is computed by

$$q = m\, c_p\, (T_{out} - T_{in}) \qquad (7.4)$$

where, q: Energy carried by the process water in Watts, m: Mass flow rate in kg/s, cp: Specific heat of water in J/(kg^{o}C), T_{out}: Exit temperature of process water in ^{o}C, T_{out}: Inlet temperature of process water in ^{o}C.

Reynolds number and Heat transfer coefficient for the test section cooling channel design at process water flow rate 1.0 L/min are 4,406 and 11,330 W/m^{2o}C, respectively. The Reynolds number and heat transfer coefficient at 1.23 L/m are 5,380 and 13,290 W/m^{2} ^{o}C respectively. The flow in the channels is transitional to turbulent.

Test 1

Heat transfer variables corresponding to flow rate of 1.23 L/min are measured when the power supply is ON and the gauge pressure varies from 0-110.32 KPa (0-16 psig). Data at flow rate 1.23 L/min plotted in Fig. 7.4 and Fig. 7.5 show heat transfer to the process water dropped at gauge pressures 55.6 KPa (8 psig), 68.95 KPa (10 psig) and 82.74 KPa (12 psig), likely due to build-up of non-condensable gases. Venting air out on the primary side at 10 psig improved the system thermal performance. Data are smooth when the flow rate is 1.01 L/min and readings are taken from 110.32-0 KPa (16-0 psig) with the power supply OFF. After the non-condensable gases are removed from the system during heater operation, the problem is not encountered during system cool-down.

Test 2

The data obtained from the second test are shown in Fig. 7.6 and Fig. 7.7. The cool down data and heat-up data are reasonably consistent. Data uncertainty limits were established in the following section indicate reported variations are within the expected range.

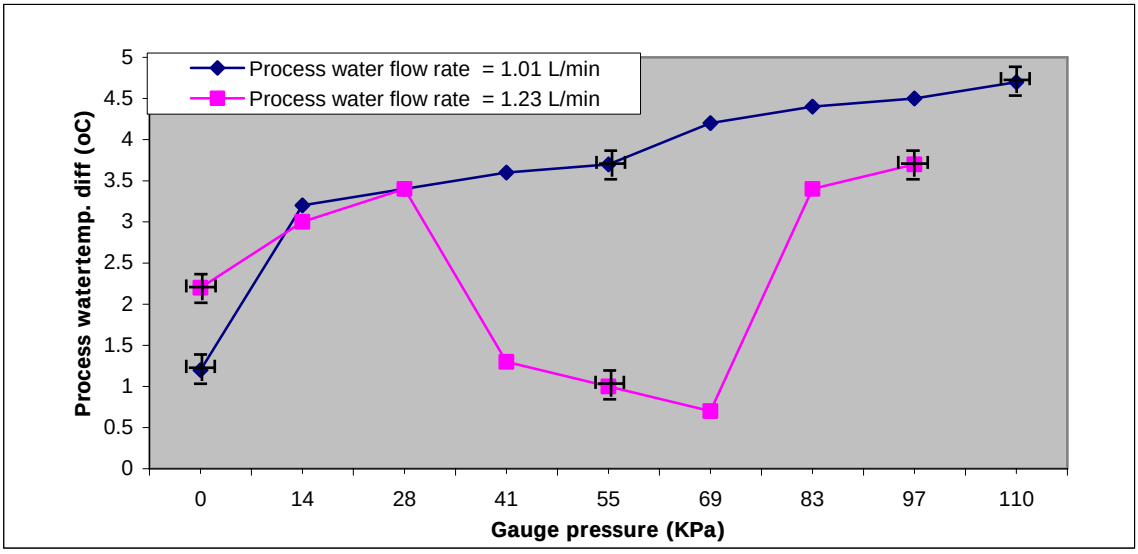

Fig. 7.4 Process water temperature difference versus gauge pressure for process water flow rate of 1.23 L/min (heat-up) and 1.01 L/min (cool-down)

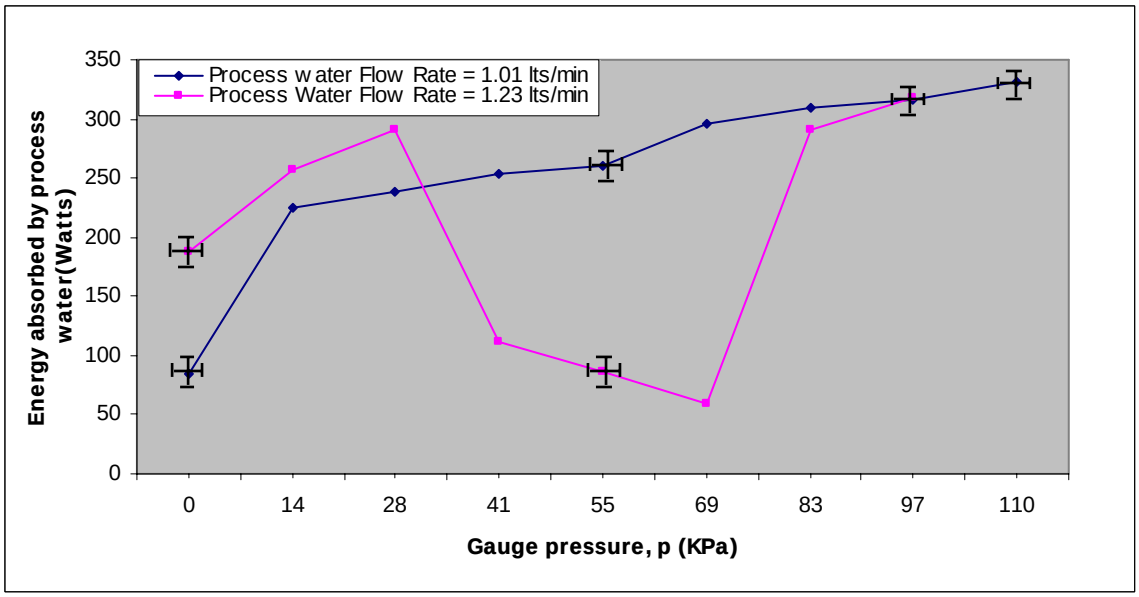

Fig. 7.5 Energy absorbed by process water versus gauge pressure for process water flow rate of 1.23 L/min (heat-up) and 1.01 L/min (cool-down)

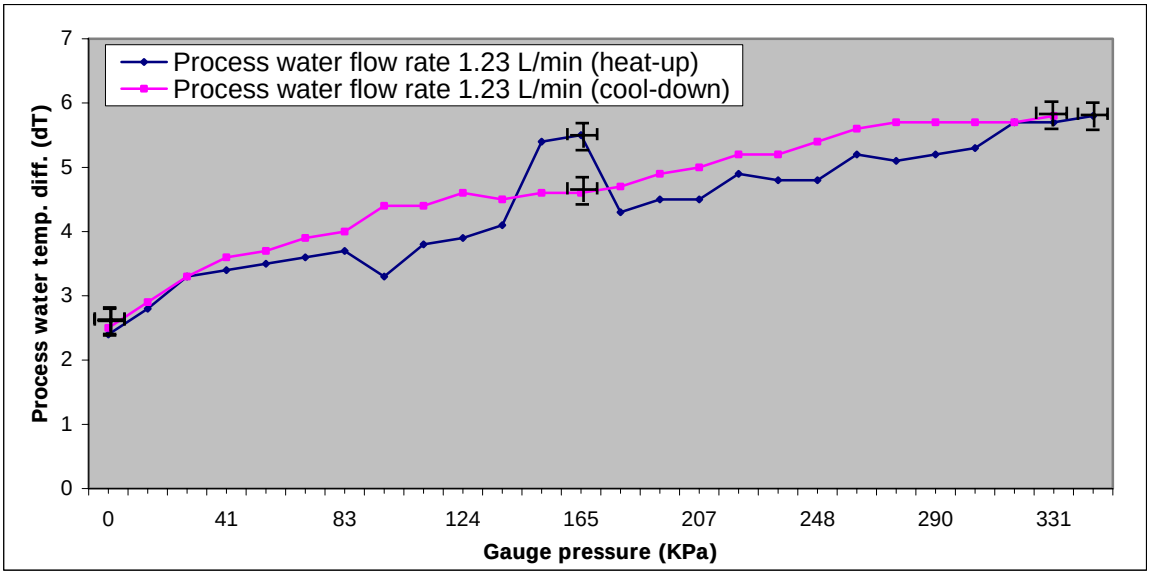

Fig. 7.6 Process water temperature difference versus gauge pressure for process water flow rate of 1.23 L/min

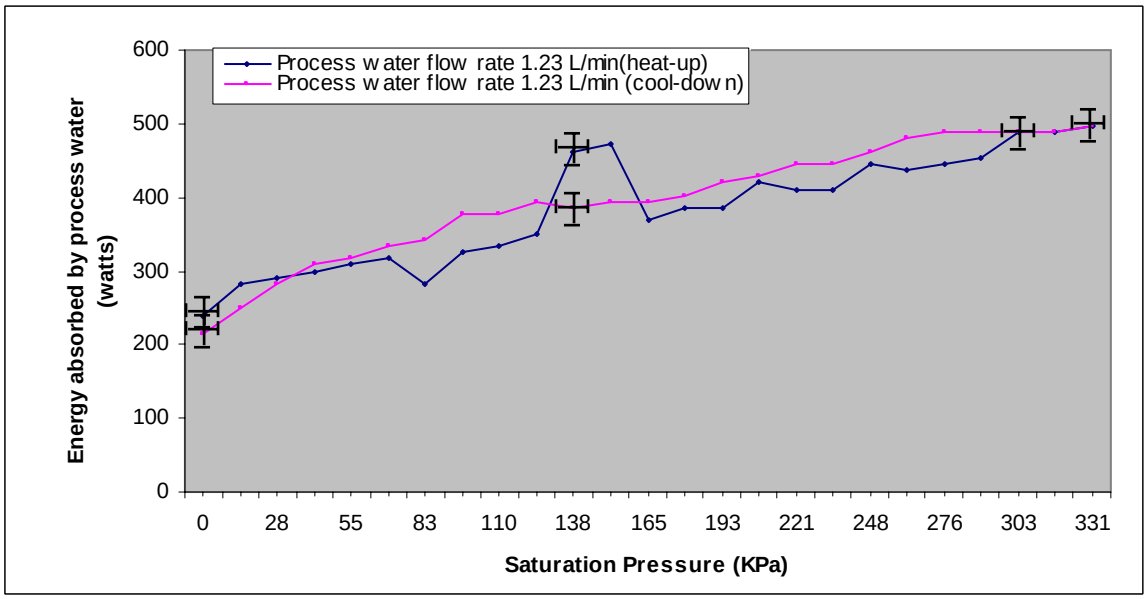

Fig. 7.7 Energy absorbed by process water versus gauge pressure for process water flow rate of 1.23 L/min

Test 3

The third test was performed at process water flow rates of 0.7 L/min, corresponding to Reynolds number 3,053 and heat transfer coefficient of 8,446 W/ m^{2o}C, with the gauge pressures varying from 0-551.6 KPa (0-80 psig). The results obtained from the third test are shown in Fig. 7.8 and Fig. 7.9. The cool-down data appears moother than that taken during the heat-up, but both heat-up and cool-down data are reasonably consistent. Summary of the results is given in table 7.2.

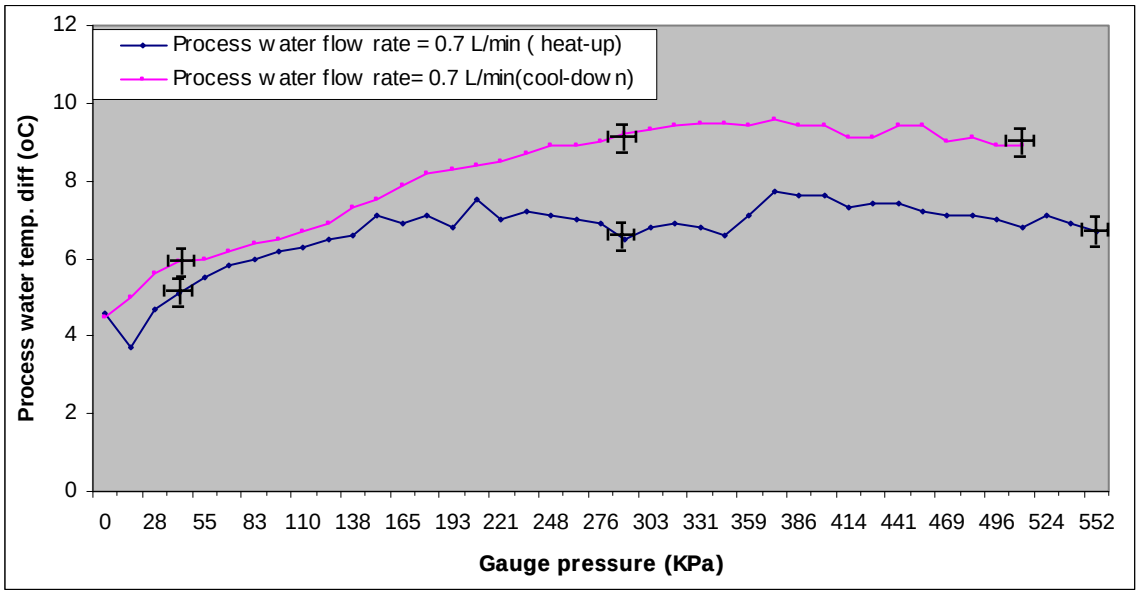

Fig. 7.8 Process water temperature difference versus gauge pressure for process water flow rate of 0.7 L/min

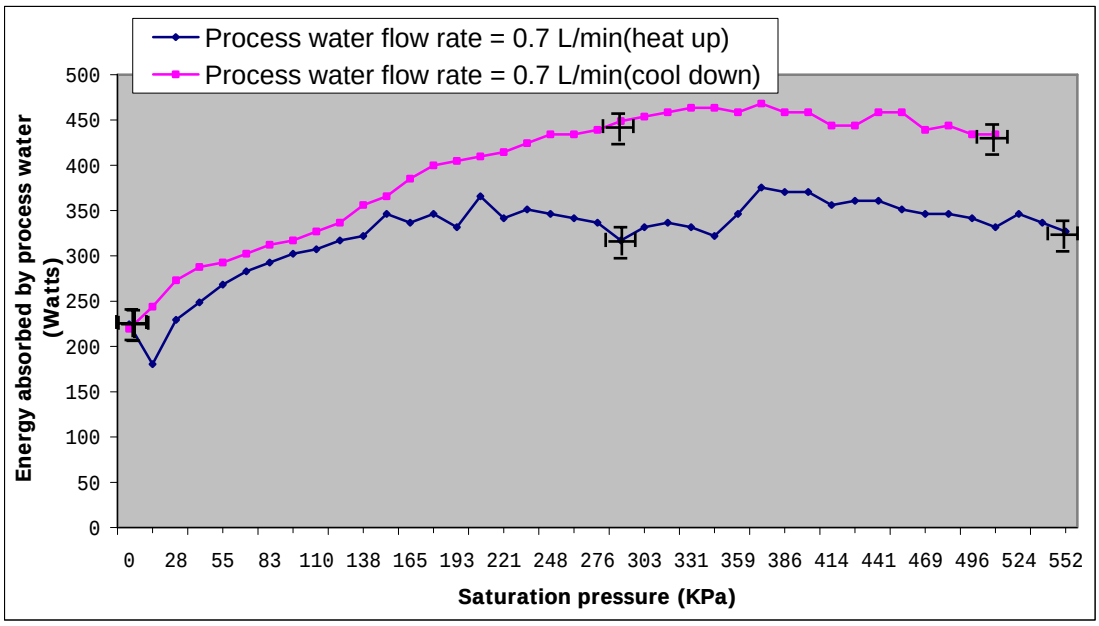

Fig. 7.9 Energy absorbed by process water versus gauge pressure for process water flow rate of 0.7 L/min

Table .7.2 Range of heat transfer variables for different process water flow rates

Process water flow rate (L/min)	Saturation pressure (KPa)	Process water temp. diff (^{o}C)	Energy absorbed by process water (Watts)
0.7 *	0-551.6	4.6-6.7	224-327
0.7**	510.23-0	8.9-4.5	434-219
1.01*	110.32-0	4.7-1.2	331-84
1.23**	13.79-110.32	2.2-3.7	189-317
1.23*	0-344.75	2.4-5.8	206-497
1.23**	330.96-0	5.8-2.5	497-214

** Heat-up state; ** Cool-down state*

7.3 Sensitivity Analysis

This analysis was performed to understand the target thermal behavior at various external heat transfer coefficient conditions. The results are given in table 7.3 and Fig. 7.10. The values given below are taken from the experimental data presented in the graphs in the previous sections. All the values are taken from the heat-up data. The target thermal behavior at prescribed pressure is examined for varying external process water flow rates. Consider case 1, where the gauge pressure is 27.58 KPa (4 psig) and the process water flow rates are 0.7 L/min, 1.01 L/min and 1.23 L/ min.

The corresponding calculated external heat transfer coefficients are 8,446 W/(m^2 ^{o}C), 11,330 W/(m^2 ^{o}C) and 13,290 W/(m^2 ^{o}C). The heat transfer coefficient will go as the

Table 7.3 Range of process water powers for different process water flow rates

Process water flow rate L/min	Reynolds number	External heat transfer coefficient W/(m^{2o}C)	Power absorbed by process water at four different gauge pressures, P (KPa)				
			P1 27.58	P2 55.16	P3 82.74	P4 110.32	P5 275.8
0.7	3,053	8,446	229	268	293	307	336
1.01	4,068	11,330	239	260	310	330	
1.23	5,380	13,290	283	300	317	471	488

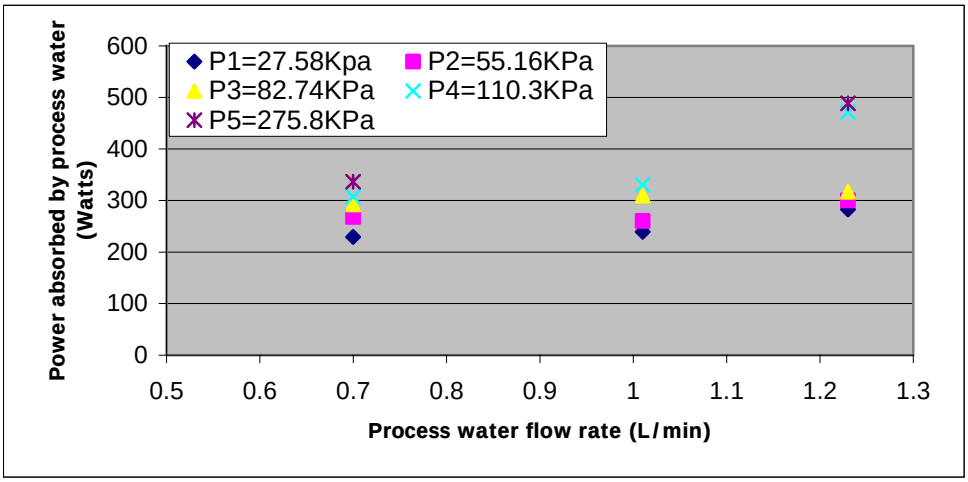

Fig. 7.10 Target thermal performance with varying external heat transfer coefficient

flow rate to the 0.8 power if the flow is fully turbulent. From the table 7.3 it can be seen that there is a significant change in the power absorbed by the process water as the flow changes from laminar to turbulent. The range of saturation temperatures is also important to the thermal performance. Thermal loss to the environment for the facility and test section is evaluated by adding the heat loss due to conduction and radiation from the MSL. Length of the MSL is taken as 0.04 m and average diameter (diameter varies due to the fittings) of MSL is taken as 0.006 m. Heat loss due to radiation is approximately 0.46 Watts and heat loss due to convection is approximately 25 watts. Therefore, the total heat loss is approximately 25.46 watts, which is not a significant variable.

7.4 Comparative Study

Computer simulations of target power were run at saturation steam pressures of 101.35 KPa (24.7 psia), 239.256 KPa (34.7 psia), 308.206 KPa (44.7 psia), 377.156 KPa (54.7 psia), 446.106 KPa (64.7 psia). These values were compared against the experimental values obtained during the heat-up state at corresponding gauge pressures of 68.95 KPa (10 psig), 137.9 KPa (20 psig), 206.85 KPa (30 psig), 275.KPa (40 psig) and 344.75 KPa (50 psig). Each gauge pressure was studied with the three different heat transfer coefficients 8,446 W/m $^{2\,o}$C, 11,330 W/m $^{2\,o}$C and 13,390 W/m $^{2\,o}$C and the results were noted. The comparative study is presented in table 7.4 and graph is shown in Fig. 7.11. The models in the simulation were unchanged, i.e., uniform heat transfer coefficient on the target external side is still employed. Theoretical results fall with in 20-30 % range of the experimental results for lower heat transfer coefficients and 30-40 % at higher heat transfer coefficients.

Table 7.4 Summary of case studies for comparative study

External heat transfer coefficient h $W/m^{2o}C$	Case 1 101.35 KPa (24.7 psia)		Case 2 239.256 KPa (34.7 psia)		Case 3 308.206 KPa (44.7 psia),		Case 4 377.156 KPa (54.7 psia)		Case 5 446.106 KPa (64.7 psia).	
	Q_{Th}	Q_{Exp}	Q_{Th}	Q_{Exp}	Q_{Th}	Q_{Exp}	Q_{Th}	Q_{Exp}	Q_{Th}	Q_{Exp}
8,446	350	283	400	322	440	366	480	336	500	322
13,390	470	308	530	351	580	386	630	437	670	497

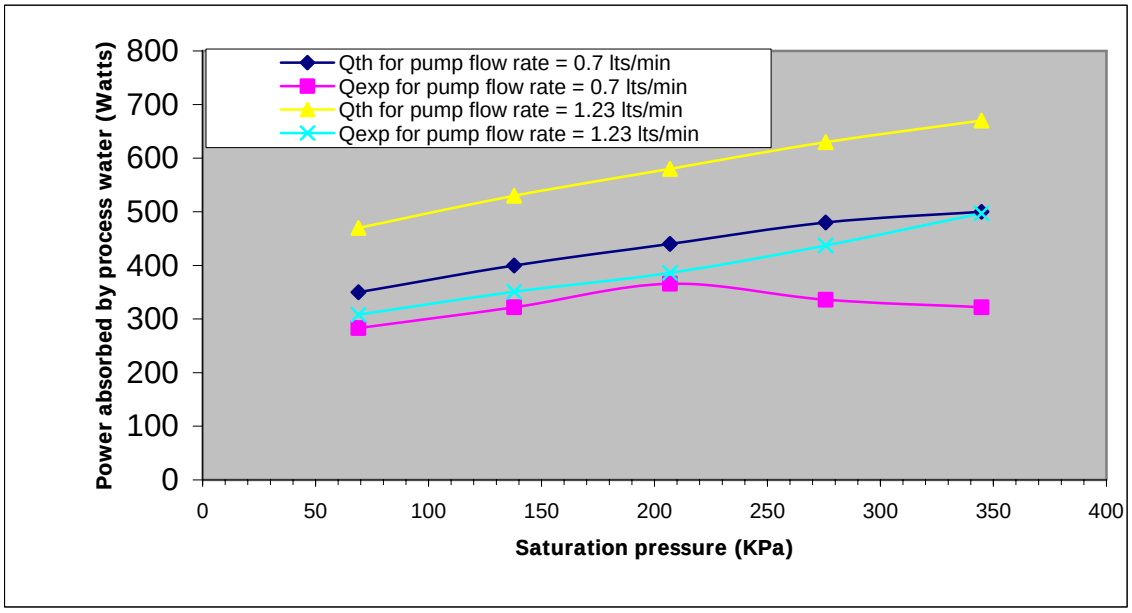

Fig. 7.11 Comparison of experimental versus theoretical target power

7.5 Future Work

The external cooling channels on the target holder do not deliver uniform flow and heat transfer. The design was adopted to promote ease of manufacture. However, the uneven heat transfer coefficient on the external surface of the target holder made the comparison of the theoretical and experimental data difficult.

The software should be modified to accommodate spatially varying external heat transfer coefficient studies. In addition, experiments at higher-pressure levels can be performed to better relate the data to the cyclotron operating conditions.

REFERENCES

A.D.Roberts, L.C. Daniel and R.J. Nickles, "A High Power Target for The Production of [^{18}F] fluoride," *Nuclear Instruments and Methods in Physics Research,* B99, 1995: 797 -799

Adrian Bejan, *Heat Transfer*, John Wiley & Sons, Inc.: New York, 1993

B.W. Wieland, D.J. Schlyer and A.P. Wolf, "Charged Particle Penetration in Gas Targets Designed for Accelerator Production of Radio nuclides Used in Nuclear Medicine," *International Journal of Applied Radiation and Isotopes*, Vol. 35, No. 5, 1984: 387-396

Das Gupta, Plowsky and Wayner, P. C., "Interfacial Force Field Characterization in a Constrained Vapor Bubble Thermosyphon," AIChE *Journal*, Vol. 41, No 9, 1995: 2140-2148.

D.A.Willis and X.Xu, "Transport Phenomena and Droplet Formation During Pulsed Laser Interaction with Thin Films," *Journal of Heat Transfer,* Vol. 22, November 2000: 763-770

Ernst U. Schlünder, *Heat Exchanger Design Handbook,* Hemisphere Pub. Corp: Washington, 1983

Fluorine18production:

http://laxmi.nuc.ucla.edu:8000/lpp/radioisotopes/radioisoprod.html

G.F. Steyn and C.J. Stevens, "The importance of Thermal Entrance Effects in Gas – Cooled Beam Windows for Radioisotope Production Targets," *Nuclear Instruments and Methods in Physics Research,* A 373, 1996: 10 – 17.

Hesselgreaves, John E, *Compact Heat Exchangers: Selection, Design, and Operation*, Pergamon: New York, 2001

Holman, J. P., *Heat Transfer*, McGraw-Hill: Fourth Edition, 1976.

Holman, J. P., *Heat Transfer*, McGraw-Hill: Eighth Edition, 1997.

Jaluria, Yogesh, *Design and Optimization of Thermal Systems*, McGraw-Hill Co.: New - York, 1998

J.M. Crye, A.E. Ruggles and W.D. Pointer, "Measurement of the Heat Transfer Coefficient for Mercury Flowing in a Narrow Channel," *Transactions of the ASME,* Vol. 124, December 2002:1034 – 1038

Khaled Meftah and A.E. Ruggles, "Vapor Volume Fraction, Flow Regime, and Vapor Velocity Inference Using Fluid Conductivity Measurements," *Review of Scientific Instruments,* AIP, Vol. 69, No 8, August 1998: 2948-2955

Lange, Jerome C., *Design Dimensioning with Computer Graphics Applications,* M. Dekker: New York, 1984

Louis Gary Lamit, *Pipe Fitting and Piping Handbook*, Prentice- Hall: New Jersey, 1949

Marc S. Berridge and Rolf Kjellström, "Designs and Use of Silver [^{18}O] Water Targets for [^{18}F] Fluoride Production, *Applied Radiation and Isotopes,* Vol. 50, 1999: 699 – 705

M. Karthikeyan, J. Huang, J. Plawsky and P.C. Wayner, Jr, "Experimental Study and Modeling of the Intermediate Section of the Nonisothermal Constrained Vapor Bubble," *Transactions of ASME*, Vol. 120. February 1998: 166-173

Merle C. Potter and John F. Foss, *Fluid Mechanics,* The Ronald Press Company: New York, 1975.

Nusselt, W.: Der Wärmeaustausch zwischen wand und Wasser im Rohr, Forsch. Geb. Ingenieurwes., vol.2, p. 309, 1931

Peter W. Wojciechowski, Munawwar Sajjad and Richard M. Lambrecht, "A Semi-Quantitative Approach to the Design, Analysis and Operation of a Gas Target system," *International Journal of Applied Radiation and Isotopes*, Vol. 39, No. 5, 1988: 429-436

Ruggles, A. E. and Alvord, C. W., "Thermal Performance Of CTI, inc. Enriched Water Targets," *Proc. 16th Int. Conf. on Application Of Accelerators In Research And Industry,* AIP, **576**, 2000:817-823.

Sampath Telikicherla Kandala, "Optimized Enriched Water Target Design for Fluorine 18 Production," *Fluids Engineering Division, ASME Summer Meeting,* Poster Session, 2003

T.C.Tszeng and V.Saraf, "A Study of Fin Effects in the Measurement of Temperature Using Surface- Mounted Thermocouples," *Transactions of the ASME,* Vol. 125, October 2003: 926 – 935

T.Köble, F. Meyer, M. Ockenfels, J. Weltz, W. Von Witsch and G. Wollmann, "The Influence of Convection on High Pressure Gas Target Densities," *Nuclear Instruments and Methods in Physics Research,* A 275, 1989: 460 - 461

Van P. Carey, *Liquid-Vapor Phase-Change Phenomena,* Taylor and Francis, 1992.

Warring, R. H., *Handbook of Valves, Piping, and Pipelines,* Gulf Publication Company: Houston, 1920.

Wu-Long Cheng, Yun Jao, Jin-Jenn Lin, Ther-Jen Ting, Jyh-Daw Sheu and Wuu-Jyh Lin, "Study on Production of Technetium – 99m Isotope with a Compact Cyclotron," *Nuclear Science Journal,* Vol. 37, No. 5, October 2000: 328 – 339.

APPENDICES

Appendix A

The following program reflux.m was written in MATLAB 6.1. The program runs on any windows based machine that has MATLAB 6.1 or higher versions. Input to the program is the target holder external heat transfer coefficient and the output is the simulation of target thermal performance.

The results of this program were explained in chapter 3. This is the baseline program for design optimization. This program is a modified version of J.M. Crye program. Condensate film models help in determining the geometry of new reflux target. The inputs with in the program are the target dimensions, target power and the thermo physical properties. This program is valid for cylindrical targets.

Algorithm for J.M. Crye Program

This program has two different options. Option 1 gives the target power as a function of vapor volume fraction. Option 2 gives detailed performance information for a single value of vapor volume fraction. This program is not presented in this thesis work but the algorithm followed by the program is presented below.

a) Define the Themophysical properties of saturated Liquid and Saturated Vapor
b) Define the maximum target power, target area and target volume.
c) Surface average flux and volume average power are calculated to provide context to the target performance envelope.
d) A single-phase natural convection heat transfer coefficient is calculated from the literature to allow estimation of the maximum target power one could deposit into the target volume without causing phase change. The target wall temperature is taken as 40 degrees.
e) The vapor mass generation and vapor volume generation are evaluated to provide context to the target flow performance.

Steps until f are common for both Study 1 and Study 2. Steps from f through k are used in Study 1 and steps from l through o are used in study 2.

f) Minimum wall temperature, T1 is defined as 40 degrees and the maximum wall temperature, T3 is 200 degrees. The mean of these two temperatures, T3 forms the estimated root. Initial error value is defined as 100.
g) The bisection method is used to solve the nonlinear equations. The wall temperature is a 1x3 matrix. Column 1 is low value (40 degrees), column 3 is

the high value (200 degrees), and column 2 is the best guess of the root and all three entries of each matrix should be very close.

h) Overall target power, Q_0 and fin power, Q_f are calculated for the three different temperature values using the corresponding heat transfer models. This is also a 1x 3 matrix. The difference between these two powers Q_d, is stored in a different matrix. This is used to estimate the new lower or higher temperature value using the following conditions.

   - ✓ if Q_d (1) * Q_d (3)>0, then the given temperature range is invalid
   - ✓ if Q_d (1) * Q_d (2)<0, then T3 = T2
   - ✓ if Q_d (1) * Q_d (2)>0, then T1 = T2
   - ✓ if Q_d (1) * Q_d (2) =0, then the root is T2 and error = 0

i) New value of T2 is calculated and the error value is calculated using the formula abs (T2-old T2)/2)*100;

j) Steps from g to i are repeated until error <= 0.1. The corresponding vapor volume fraction and overall target power are stored in a matrix.

k) Steps from f to j are repeated for vapor volume fractions ranging from 0 through 1 and the required plot is drawn.

l) Value of the vapor volume fraction is entered.

m) Condensation heat transfer coefficient as a function of wall temperature is plotted. In fact, this does not depend on vapor volume fraction.

n) Single-phase power, condensation power, overall power and the ratio of condensation power to the over all power are plotted against the wall temperatures.

o) Fin power as a function of wall temperature is plotted.

Inventory Based Program for Optimization

a) Define the Themophysical properties of saturated Liquid and Saturated Vapor

b) Define the target dimensions.

c) Define the target volume.

d) Input the target holder external heat transfer coefficient.

e) The target power range is predefined and can be varied according to the vapor volume fraction that is obtained from the output. The maximum vapor volume fraction is desired is 84 % of the total target volume since 0.16 cc of liquid should be available for the beam stop. This 84 % includes the condensate film, and the condensate in transit between the draining film and the beam impingement volume.

f) Condensate volume fraction, Vapor volume fraction, Condensate film thickness, Heat transfer area for condensation are plotted against target power those are discussed in the results section. The software has been validated against the older version used to evaluate the performance of the baseline RDS-111 target. The software version given in Appendix A has the input for that validation.

%Thermal Performance of CTI Target: Reflux Target Design

```
%  Models developed by Dr. Ruggles and Sampath T.K

%  MATLAB program showing the relation between liquid film area
% and Liquid film volume as a function of vapor volume generated and
%  the percentage of vapor volume in the total liquid volume.

%  This evaluation considers the fluid in the target holder as a
%  fixed control volume.  The system is at steady state and the
%  target wall temperature is taken as uniform inside the holder.
%  The system is saturated at 681 psia based on operating documents
%  from CTI. The target window is taken as an insulated boundary.
%
%  The liquid film on the wall is obtained by the condensation of
%  the vapor in the upper portion of the target. The flow of liquid
%  in the film is considered to be LAMINAR.The sources for equations which are
%  used to calculate thickness of the film followed by the area and
%  volume of the film as a function of vapor volume are given in the body of the
%  thesis

%  Liquid and vapor saturation properties are given below in SI units:

%  ****************************************************************
rowl=784;          %kg/m^3     Liquid Density
mul=104.8E-6;      %kg/(m*s)   Liquid Viscosity
kl=.603;           %W/(m*c)    Liquid Thermal Conductivity
prl=0.866;         %           Liquid Prandtl Number
rowv=23.7;         %kg/m^3     Vapor Density
tsat=260;          %degrees C  Saturation Temperature
psat=681*6895;     %Pa         Saturation Pressure
hfg=1661000;       %J/kg       Latent Heat of Condensation of Vapor
l=0.005;           %m          Characteristic Length of the Film
g=9.8;

silvarea=3.14*0.0059*2*0.008+3.14*0.005^2;
%(m^2    Heat Transfer Area to Silver Estimated)

disp('Enter the number of graph you want to plot:');
disp('---1: Detailed study for different target powers');
disp('---2: Exit');
sel = input('Type the number of the graph you want: ');

% sel=1----> Detailed study for different target powers
```

```
if sel == 1

hout=input('Enter the Single Phase Heat Transfer Coefficient(5000,..):');

i=1;
for qt=300:50:700       %Different Target Powers

 totalvol=3.14*0.0059^2*0.008;
 mdotv=qt/hfg;          %kg/s  Vapor Mass Generation Rate
 vdotv=mdotv/rowv;      %m^3/s Vapor Volume Generation Rate
 l=0.005;               %m Characteristic Condensation Length
 ph=0.022*3.14;         %m Heated Perimeter of Cylindrical Fin
 ks=400;                % W/(m*C)Silver Thermal Conductivity
 tout=40;
 %C  Avg Bulk Temp of Process Cooling Water. =(Tin+Tout)/2
 lf=0.076;                                %m Length of Fin
 ac=3.14*(0.022^2)*0.25;                  %(m^2) Cross-sectional Area of Target Holder(fin)
 mf=(hout*ph/(ks*ac))^(1/2);              %Group in Fin Theory from Holman
 ma=(hout*ph*ks*ac)^(1/2);                %Group in Fin Theory from Holman
 twall(i)=(tout)+(qt/(tanh(mf*lf)*(ma)));
 % The above formula for twall is obtained by equating qtarget to qfinPower

 num1=1.13*(rowl*(rowl-rowv)*g*hfg*(kl^3))^(1/4);
 % Numerator in hconden formula
 den1=(l.*mul.*(tsat-twall(i))).^(1/4);
 % Denominator in hconden formula
 hconden(i)=num1./den1;
 % W/(m^2*C)hconden is condensation heat transfer coefficient

 velv=vdotv/(0.5*0.008*0.0118);      % m/s  Velocity of Vapor
 vell=velv;
 rel= (rowl*vell*l)/mul;             % Reynolds Number
 Nul= 0.023*(rel^0.8)*(prl^0.4);     % Nusselt Number
 hspl=Nul*kl/l;
 % W/(m^2*C) Single Phase Heat Transfer Coefficient
 num2=((qt)-(hspl*silvarea*(tsat-twall(i))));
 % Numerator in alpha formula
 den2=(hconden(i)*(tsat-twall(i))*silvarea)-(hspl*silvarea*(tsat-twall(i)));
 % Denominator in alpha formula
 alpha(i)=num2/den2;
 % This formula is obtained by substituting the twall obtained above in
 % the qtarget formula in Holman
 areafilm(i) = (silvarea.*alpha(i));
 deltaf(i)=((4*mul*l*kl*(tsat-twall(i))./(hfg*g*rowl*(rowl-rowv))).^(1/4));
 volfilm(i)=areafilm(i).*deltaf(i);
```

```
alphafilm(i)=(volfilm(i)./totalvol);
alphar(i)=alpha(i)-alphafilm(i);
z(i)=qt;
i=i+1;
end  % Ends for statement

figure(1);
set(gcf,'Color',[0.3,0.4,0.6])
plot(alphafilm,z,'go-','linewidth',1);
grid on;
zoom on;
xlabel('Condensate Volume fraction(alphafilm)-----X');
ylabel('Target Power(qt(W))-----Y');
title(['Target power(qt) Vs Condensate Volumefraction(alphafilm)'...
    'for hout=',num2str(hout),'W/(m^2*C)']);

figure(2);
set(gcf,'Color',[0.3,0.4,0.6])
plot(alpha,z,'go-','linewidth',1);
grid on;
zoom on;
xlabel('vapor volume fraction(alpha)-----X');
ylabel('Target Power(qt(W))-----Y');
title(['Target power(qt) Vs Vapor Volumefraction(alpha)'...
      'for hout=',num2str(hout),'W/(m^2*C)']);

figure(3);
set(gcf,'Color',[0.3,0.4,0.6])
plot(deltaf,z,'go-','linewidth',1);
grid on;
zoom on;
xlabel('Condensate film thickness(deltaf(m))-----X');
ylabel('Target Power(qt(W))-----Y');
title(['Target power(W) Vs condensate film thickness(m)'...
      'for hout=',num2str(hout),'W/(m^2*C)']);

figure(4);
set(gcf,'Color',[0.3,0.4,0.6])
plot(areafilm,z,'go-','linewidth',1);
grid on;
zoom on;
xlabel('Heat Transfer Area for condensation((areafilm(m^2))-----X');
ylabel('Target Power(qt(w))-----Y');
title(['Target power(W) Vs Heat Transfer area for condensation(m^2)'...
      'for hout=',num2str(hout),'W/(m^2*C)']);
```

```
 figure(5);
 set(gcf,'Color',[0.3,0.4,0.6])
 plot(twall,alpha,'ro-','linewidth',1);
 grid on;
 zoom on;
 xlabel('Wall Temperature(twall(degree- centigrade))-----X');
 ylabel('vapor volume fraction(alpha)-----Y');
 title(['Vapor Volume fraction(alpha) Vs Wall temperature(twall)'...
        'for hout=',num2str(hout),'W/(m^2*C)']);

 figure(6);
 set(gcf,'Color',[0.3,0.4,0.6])
 plot(alphar,alphafilm,'ro-','linewidth',1);
 grid on;
 zoom on;
 xlabel('Real Vapor volume Fraction(alphar)-----X');
 ylabel('Condensate volume fraction(alphafilm)-----Y');
 title(['Condensate volume fraction(alphafilm) Vs Real Vapor'....
        'volume Fraction(alphar)for hout=',num2str(hout),'W/(m^2*C)']);

elseif sel == 2
   break
end
```

Appendix B

The following program optreflux.m was written in MATLAB 6.1. The program runs on any windows based machine that has MATLAB 6.1 or higher versions. Input to the program is the target holder external heat transfer coefficient and the output is the graphs that simulate the thermal performance of the optimized target.

This program is a modified version of the program given in Appendix A. The difference in the two programs is the models that are used for the heat transfer areas. Heat transfer models for a cylindrical geometry was employed in the previous program where as for the current program, the condensation dome is taken as triangular region with a ridge and the beam stop region is taken as semi-circular cavity. Models for these geometries were derived and updated in the program. Target dimensions were altered until near optimum was achieved. The results of this program were explained in chapter 4. The inputs with in the program are the target dimensions, target power and the thermo physical properties.

Thermal Performance of CTI Target: Optimized Reflux Target Design

```
% Thermophysical properties for Un-enriched water @680 psia

rowl=784;          %kg/m^3  Liquid Density
mul=104.8E-6;    %kg/(m*s)Liquid Viscosity
kl=0.603;          %W/(m-C) Liquid thermal conductivity
prl=0.866;         %Liquid  Prandtl Number
rowv=23.7;         %kg/m^3  Vapor Density
tsat=260;          %C  Saturation Temperature
psat=680*6895;   %Pa Saturation Pressure
hfg=1661000;     %J/kg    Latent Heat of Condensation of Vapor
g=9.8;

rtf=0.005;           %m Radius of the Target Front
ltf=0.003;           %m Length of the Target Front
bcd=0.01;            %m Base of the Condensation Triangle Dome
shcd=0.01;           %m Slant Height of the Condensation Dome
vhcd=0.866*bcd;   %m Vertical Height of the Condensation Dome
lf=0.03;             %m Length of the Fin
bb=0.0025;


v1= (0.5*3.14*(rtf^2)*ltf);
%m^3 Volume of Bottom Target Front
v2= (0.5*bcd*0.866*bcd*(lf-ltf));
%m^3 Volume of Forward Condensation Dome
v3= (0.5*bcd*0.866*bcd*ltf);
%m^3 Volume of Backward Condensation Dome
v4= (0.5*0.5*bcd*0.866*0.5*bcd*(lf-ltf));
%m^3 Volume of the Ridge
vtotal=v1+v2+v3-v4;

atf= 3.14*rtf*ltf;
%m^2 Surface Area of the Target Front
acd= (2*shcd*ltf)+(((2*shcd)+(2*bb)+(2*0.5*bcd))*(lf-ltf));
%m^2 Surface Area of the Condensation Dome
ab= 3.14*rtf^2;
%m^2 Surface Area of the Target Back
as=atf+acd+ab;
%m^2 Estimated Heat transfer Area to Silver


disp('Enter the number of graph you want to plot:');
```

```
disp('---1: Detailed study for different target powers');
disp('---2: Exit');
sel = input('Type the number of the graph you want: ');

% sel=1----> Detailed study for different target powers

if sel == 1
hout=input('Enter the single phase heat transfer coefficient(5000..):');

i=1;
h=0;
for qt=0:10:1000          %Different Target Powers

 mdotv=qt/hfg;            %kg/s  Vapor Mass Generation Rate
 vdotv(i)=mdotv/rowv;  %m^3/s Vapor Volume Generation Rate
 l=0.01;                  %m Characteristic Condensation Length
 ph=0.022*3.14;           %m Heated Perimeter of Cylindrical Fin
 ks=400;                  %W/(m-C)Silver Thermal Conductivity
 tout=40;                 %C Cooling Water Temperature
 mw=2/60;                 %2 lts/sec Mass of Coolant
 cp= 4.18 * 10^3;         %J/(kg-C)  Specific Heat of Water
 t=60;

 tmean=((2*tout)+(qt/(mw*cp)))/2;
 %C Avg Bulk temp of process cooling water.  =(Tin+Tout)/2
 hf=0.076;                          % m Height of Fin
 ac=3.14*(0.022^2)*0.25;
 % (m^2) Cross-Sectional Area of Target Holder (fin)
 mf=(hout*ph/(ks*ac))^(1/2);   % Group in Fin Theory from Holman
 ma=(hout*ph*ks*ac)^(1/2);    % Group in Fin Theory from Holman
 twall(i)=(tmean)+(qt/(tanh(mf*hf)*(ma)));


 num1=1.13*(rowl*(rowl-rowv)*g*0.866*hfg*(kl^3))^(1/4);
 den1=(l.*mul.*(tsat-twall(i))).^(1/4);
 hconden(i)=num1./den1;


 velv(i)=vdotv(i)/((0.5*bcd*0.866*bcd)-(0.5*0.5*bcd*0.866*0.5*bcd));
 vell(i)=0.002;
 rel= (rowl*vell(i)*l)/mul;                    % Reynolds Number
 Nul= 0.023*(rel^0.8)*(prl^0.4);             % Nusselt Number
 hspl(i)=Nul*kl/l;
 % W/(m^2-C) Single Phase Heat Transfer Coefficient
  if h<=0.00433
```

```
 num2=((qt-(hspl(i).*(tsat-twall(i))*(atf+acd)))^2)*0.866;
den2=((((hconden(i)-hspl(i))*(tsat-twall(i))*2)^2))*(2*vtotal*lf);
alpha(i)=num2/den2;
areafilm(i) = ((2*alpha(i)*vtotal./ 0.866*lf)^(1/2))*(2*lf);
else
num2=((qt-(hspl(i)*(tsat-twall(i))*(atf+acd)))^2)*((0.433*lf)-(0.10825*(lf-ltf)))*4.7;
den2=(((hconden(i)-hspl(i))*(tsat-twall(i))*((4*lf)+0.006-(4*ltf)))^2)*(vtotal);
alpha(i)=num2/den2;
areafilm(i) = ((alpha(i)*vtotal./1.56*lf)^(1/2))*(4*lf-(2*ltf));
end

b1=((2.*alpha(i).*vtotal)./(0.866*lf))^(1/2);
h(i)= 0.866*b1;

 % Module VIII
 % Calculation of Film Thickness
 % See Chapter 2.6 of the Program Reference

 deltaf(i)=((4*mul*l*kl*(tsat-twall(i))./(hfg*g*rowl*(rowl-rowv))).^(1/4));
 % m Condensate Film Thickness

 volfilm(i)=areafilm(i).*deltaf(i);   %m^3 Condensate Volume
 alphafilm(i)=(volfilm(i)./vtotal);   % Condensate Volume Fraction
 alphar(i)=alpha(i)-alphafilm(i);     % Real Volume Fraction
 z(i)=qt;

 vbs=(3.14*0.5*rtf^2*ltf);            %m^3 Beam Stop Volume
 vvap(i)=(alpha(i)*vtotal);           %m^3 Vapor Volume
 mbs=(3.14*0.5*rtf^2*ltf)*rowl;       %Kg Beam Stop Mass
 mfilm(i)=rowl*volfilm(i);            %Kg Mass of Condensate Film
 mvap(i)=(alpha(i)*vtotal)*rowv;%kg Mass of vapor
 a(i)=mbs+mfilm(i)+mvap(i);
 % The value of "a" is calculated to have an idea of the mass of the
 % liquid in different regions.  It is not used for plotting any graphs.

 retvol(i)=vtotal-(vbs + vvap(i) + volfilm(i));
 %m^3 Volume of Liquid from Return Channel
 mret(i)=retvol(i).*rowl;
 %kg Mass of Liquid from Return Channel

 i=i+1;

end

 figure(1);
```

```
plot(alpha,z);
grid on;
zoom on;
xlabel('Vapor volume fraction(alpha)-----X');
ylabel('Target Power(qt(W))-----Y');
title(['Target power(qt) Vs Vapor Volumefraction(alpha)'...
    'for hout=',num2str(hout),'W/(m^2*C)']);

text(0.083,970,'\bullet\fontname{times}','FontSize',18);
figure(2);
plot(twall,z);
grid on;
zoom on;
xlabel('Wall temperature(twall(degree C)-----X');
ylabel('Target Power(qt(W))-----Y');
title(['Target power(qt) Vs Wall Temperature(Twall)'...
    'for hout=',num2str(hout),'W/(m^2*C)']);
text(138.1566,970,'\bullet\fontname{times}','FontSize',18);

figure(3);
plot(alphar,z);
grid on;
zoom on;
xlabel('Real vapor volume fraction(alphar)-----X');
ylabel('Target Power(qt(W))-----Y');
title(['Target power(qt) Vs Real vapor volume fraction(alphar)'...
    'for hout=',num2str(hout),'W/(m^2*C)']);
text(0.0832,970,'\bullet\fontname{times}','FontSize',18);



figure(4);
plot(z,retvol);
grid on;
zoom on;
xlabel('Target Power(qt(W))-----Y');
ylabel('Return volume through both channels(retvol(m^3))-----X');
title(['Return volume through both channels(retvol) Vs Target power(qt)'...
    'for hout=',num2str(hout),'W/(m^2*C)']);
text(970,9.1247e-007,'\bullet\fontname{times}','FontSize',18);

figure(5);
plot(velv,z);
grid on;
zoom on;
```

```
 xlabel('Vapor velocity(velv(m/s))-----X');
 ylabel('Target Power(qt(W))-----Y');
 title(['Target power(qt) Vs Vapor Velocity(velv)'...
      'for hout=',num2str(hout),'W/(m^2*C)']);

end
```

VITA

Sampath Telikicherla Kandala was born on August 11, 1981 in Kakinada, India. Since his father works for a bank, he pursued his schooling in several places in India. Inspired by his fascination for Automobiles, he chose to major in Mechanical Engineering and graduated with a Bachelor of Technology in Mechanical Engineering in April 2002. He graduated in first position from Gokaraju Rangaraju Institute of Engineering and Technology (GRIET), an affiliated college to Jawaharlal Nehru Technological University (JNTU), Hyderabad - India. During his Bachelors study, he is the only recipient of one Gold Medal and two Silver Medals for academic excellence in Mechanical Engineering.

In August 2002, he joined The University of Tennessee (UT), Knoxville to pursue Master of Science in Mechanical Engineering while working as a Graduate Research Assistant for Dr. Arthur E. Ruggles. As a graduate student at the UT, Sampath performed research on Enriched Water Targets for CTI, Inc. Sampath was awarded R.N. Lyon Fellowship by the college of engineering for outstanding thermal sciences research. Currently, he is working on a collaborate project with Dr. Jack Wasserman and Dr. Lumsdaine in Hand - Arm Vibrations (HAV). Current research involves developing damping techniques to reduce the HAV of a tool. He will be graduating in summer 2004.